

SILICON NANOWIRES FOR NETWORK PHOTODETECTORS AND PLASMONIC  
APPLICATIONS

A THESIS SUBMITTED TO  
THE GRADUATE SCHOOL OF NATURAL AND APPLIED SCIENCES  
OF  
MIDDLE EAST TECHNICAL UNIVERSITY

BY

EMRE MÜLAZIMOĞLU

IN PARTIAL FULFILLMENT OF THE REQUIREMENTS  
FOR  
THE DEGREE OF MASTER OF SCIENCE  
IN  
METALLURGICAL AND MATERIALS ENGINEERING

JULY 2013



Approval of the thesis:

**SILICON NANOWIRES FOR NETWORK PHOTODETECTORS AND  
PLASMONIC APPLICATIONS**

submitted by **EMRE MÜLAZIMOĞLU** in partial fulfillment of the requirements for the degree of **Master of Science in Metallurgical and Materials Engineering Department, Middle East Technical University** by,

Prof. Dr. Canan ÖZGEN  
Dean, Graduate School of **Natural and Applied Sciences**

\_\_\_\_\_

Prof. Dr. C. Hakan GÜR  
Head of Department, **Metallurgical and Materials Engineering**

\_\_\_\_\_

Assoc. Prof. Dr. H. Emrah ÜNALAN  
Supervisor, **Metallurgical and Materials Eng. Dept., METU**

\_\_\_\_\_

**Examining Committee Members:**

Prof. Dr. Tayfur ÖZTÜRK  
Metallurgical and Materials Eng. Dept., METU

\_\_\_\_\_

Assoc. Prof. Dr. H. Emrah ÜNALAN  
Metallurgical and Materials Eng. Dept., METU

\_\_\_\_\_

Prof. Dr. Raşit TURAN  
Physics Dept., METU

\_\_\_\_\_

Assoc. Prof. Dr. Caner DURUCAN  
Metallurgical and Materials Eng. Dept., METU

\_\_\_\_\_

Assist. Prof. Dr. Y. Eren KALAY  
Metallurgical and Materials Eng. Dept., METU

\_\_\_\_\_

**Date:** 11/07/2013

**I hereby declare that all information in this document has been obtained and presented in accordance with academic rules and ethical conduct. I also declare that, as required by these rules and conduct, I have fully cited and referenced all material and results that are not original to this work.**

Name, Last Name: Emre MÜLAZIMOĞLU  
Signature :

## ABSTRACT

### SILICON NANOWIRES FOR NETWORK PHOTODETECTORS AND PLASMONIC APPLICATIONS

MÜLAZIMOĞLU, Emre

M. Sc., Department of Metallurgical and Materials Engineering

Supervisor: Assoc. Prof. Dr. H. Emrah ÜNALAN

Co-Supervisor: Prof. Dr. Raşit TURAN

July 2013, 56 Pages

Being the key component of the semiconductor industry, silicon in nanowire form has gained increased attention. In this thesis, vertical arrays of silicon nanowires (Si NWs) have been fabricated with metal assisted etching method (MAE). MAE method is a simple, solution based and low temperature process. In this method, fabricated nanowires inherit the starting wafer characteristics, such as doping type, density and crystal orientation.

In the first part, fabricated NWs in network form have been demonstrated as the active layer in metal-semiconductor-metal photodetectors. Devices showed partial transparency and fully reversible switching behavior. Moreover, fast dynamic response has been obtained with 0.43 milliseconds for the rise time and 0.58 milliseconds for the fall time. Flexible PDs were fabricated on polyethylene-terephthalate substrates and operational during bending up to a radius of 1 cm.

In the second part, surface plasmon resonance properties of the silver (Ag) nanoparticle decorated Si NWs have been investigated. Si NWs were fabricated through one-step and two-step MAE method. Two-step MAE method involved the use of hydrogen peroxide. Ag nanoparticles were decorated onto Si NWs through simple evaporation and annealing processes. The hydrogen peroxide in MAE method was found to degenerate the surface of nanowires and created oxygen defects. Defects enhanced infrared absorption at higher frequencies and led to emission of light by radiative recombination. Almost 50-fold enhanced localized-surface-plasmon-resonance (LSPR) was obtained. It was attributed to the change in the dielectric constant of effective medium. LSPR wavelength could be tuned by changing Ag particle size and NW length.

*Keywords:* Silicon nanowires, photodetectors, surface plasmon resonance

## ÖZ

### SİLİSYUM NANOTELLERİN AĞ YAPILI IŞIK DETEKTÖRİNDE KULLANILMASI VE PLAZMONİK UYGULAMALARI

MÜLAZIMOĞLU, Emre

Yüksek Lisans, Metalurji ve Malzeme Mühendisliği Bölümü

Tez Yöneticisi: Doç. Dr. H. Emrah ÜNALAN

Ortak Tez Yöneticisi: Prof. Dr. Raşit TURAN

Temmuz 2013, 56 Sayfa

Yarıiletken endüstrisinin en önemli yapıtaşı olan silisyum nanotel formunda da son zamanlarda yoğun olarak araştırma konusu olmuşlardır. Bu tez çalışmasında, dik olarak hizalanmış silisyum nanoteller (Si NWs) metal yardımcı dağlama (MYD) yöntemi ile üretilmişlerdir. Bu metod basit bir yöntem olup çözelti tabanlı ve düşük sıcaklık prosesi olması sebebiyle oldukça yaygınlaşmıştır. Bu metod ile üretilen nanoteller başlangıç substratı ile aynı aşılama tipi ve yoğunluğu gibi temel özelliklere sahiptir.

Bu tez çalışmasının ilk kısmında, üretilen nanoteller ağ halinde metal-yarıiletken-metal ışık detektörlerinin aktif kısmında kullanılmışlardır. Üretilen detektörler kısmi transparanlık ve tekrar edilebilir açılıp kapanma özelliği göstermişlerdir. Buna ek olarak, detektörlerin açma ve kapanma hızları 0.43 milisaniye ve 0.58 milisaniye olarak belirlenmiştir. Esnek detektörler ise kullanılan substratın PET ile değiştirilmesi sonucu üretilmişlerdir. Üretilen esnek detektörler 1 santimetrelük yarıçapa kadar bükülme testine tabi tutulmuş olup bükülme sırasında da çalışmaya devam etmişlerdir.

Tez çalışmasının ikinci kısmında ise gümüş (Ag) nanoparçacıklar ile dekore edilmiş dik hizalanmış silisyum nanoteller yüzey plazmon rezonansı özellikleri açısından incelenmiştir. Silisyum nanoteller tek adım ve iki adım MYD metodu ile üretilmişlerdir. İki adım MYD metodu hidrojen peroksit kullanımını içermektedir. Gümüş nanoparçacıklar ise buharlaştırma ve tavlama yöntemi ile nanoteller üzerinde oluşturulmuşlardır. İki adım metodu nanotellerin yüzeyini deforme ederek oksijen kaynaklı kusurlar yaratmışlardır. Bu kusurlar yüksek frekanstaki kızılötesi ışıkları absorbe etmekte olup ışınımlı rekombinasyon ile ışık yayabilmektedirler. Yaklaşık 50 kata kadar artmış lokalize yüzey plazmon rezonansı (LYPR) elde edilmiştir. Bu artış nanotellerin yüzeyinde bulunan oksijen kaynaklı kusurların ortamın dielektrik katsayısını değiştirmesi ile ilintilendirilmiştir. Rezonans dalgaboyu gümüş nanoparçacıkların büyüklüğü ve nanotellerin uzunluğu ile değiştirilebilmektedir.

*Anahtar kelimeler:* Silisyum nanoteller, ışıkdetektörleri, yüzey plazmon rezonansı

*All that is gold does not glitter,  
Not all those who wander are lost;  
The old that is strong does not wither,  
Deep roots are not reached by the frost.*

*From the ashes a fire shall be woken,  
A light from the shadows shall spring;  
Renewed shall be blade that was broken,  
The crownless again shall be king.*

*JRR Tolkien*

## ACKNOWLEDGEMENTS

This thesis is an interdisciplinary work between departments of Physics and Metallurgical and Materials Engineering in METU.

I would like to express my deepest thanks to my supervisor Assoc. Prof. Dr. H. Emrah Ünalán for his guidance, help and patience. I would also like to thank my co-supervisor Prof. Dr. Raşit Turan for his valuable advices and supervision.

Throughout this thesis, I am thankful to Serkan Yılmaz, Mete Günöven, Gizem Nogay, Bayram Bütün and Prof. Dr. Ekmel Özbay for their help in the characterization setups.

I owe my deepest gratitude to my lab-mates and friends Şahin Coşkun, Ayşegül Afal, Burcu Aksoy, Recep Yüksel, Zeynep Sarıoba, Elif Selen Ateş, and Şeyda Küçük yıldız for their infinite support, patience and kindness. I will never forget the time we have had together and I feel very lucky to get to know such great people. I am also grateful to Barış Özdemir and Mustafa Kulakçı. They were always willing to help to me. I also have to mention Mehmet Yıldırım, Burak Aktekin, Kıvanç Yurdakul, Fuat Erden, Can Yıldırım, Güzde Alkan, Tümerkan Kesim and Hakan Yavaş for their support and beautiful friendship.

Yasemin Gizem Fillik. I am so grateful for your infinite support. Thanks for standing back of me when I needed it.

Finally, I would like to express my endless thanks and gratitude to my sister, my mom and dad. Without their love, patience and support I would not have been able to complete this thesis. After spending 7 years at METU, it is time for a change. Delft, here I come!

## TABLE OF CONTENTS

ABSTRACT.....	v
ÖZ .....	vi
ACKNOWLEDGEMENTS .....	viii
TABLE OF CONTENTS .....	ix
LIST OF FIGURES .....	xi
CHAPTERS .....	1
1. INTRODUCTION .....	1
1.1 FEATURES OF NANOMATERIALS .....	1
1.1.1 Thermal, Electrical, Optical and Magnetic Properties of Nanomaterials.....	1
1.1.2 Nanowires as 1D Nanomaterials.....	4
1.2 FABRICATION OF Si NWS .....	5
1.2.1 Bottom-Up Approach for the Fabrication of Si NWs .....	5
1.2.2 Top-Down Methods For the Fabrication of Si NWs.....	7
1.3 EMERGING APPLICATIONS OF Si NWS.....	12
1.3.1 Field Effect Transistors (FETs).....	12
1.3.2 Heterojunction Solar Cells .....	13
2. SILICON NANOWIRE NETWORK METAL-SEMICONDUCTOR-METAL (MSM) PHOTODETECTORS .....	19
2.1 INTRODUCTION .....	19
2.1.1 NW Configurations used in Photodetection.....	19
2.1.2 Major Photodetector types for Si NWs .....	21
2.1.3 Si NW Architectures Used In Photodetector Applications .....	22
2.2 EXPERIMENTAL DETAILS .....	24
2.2.1 Fabrication of Nanowires.....	24
2.2.2 Fabrication of Photodetectors .....	25
2.3 CHARACTERIZATION METHODS.....	26
2.3.1 Scanning Electron Microscopy .....	26
2.3.2 Electrical Characterization.....	26
2.3.3 Optical Characterization .....	26

2.4	RESULTS.....	26
2.4.1	Fabrication of Si NWs and Vacuum Filtration Technique .....	26
2.4.2	Density Calculation of NWs and Transmittance result.....	27
2.4.3	Device Characterization .....	28
2.4.4	Flexible MSM Photodetector .....	31
3.	SILVER NANOPARTICLE DECORATED SILICON NANOWIRES FOR LOCALIZED SURFACE PLASMON RESONANCES .....	33
3.1	INTRODUCTION.....	33
3.1.1	Light and Metal Nanoparticle Interactions.....	33
3.1.2	Localized Surface Plasmon Resonances .....	34
3.2	EXPERIMENTAL DETAILS .....	36
3.2.1	Fabrication of Nanowires .....	36
3.2.2	Silver Nanoparticle Decoration.....	36
3.3	CHARACTERIZATION METHODS .....	36
3.3.1	Scanning Electron Microscopy (SEM) .....	36
3.3.2	Transmission Electron Microscopy (TEM).....	36
3.3.3	Reflectance Measurements .....	37
3.3.4	Fourier Transformed Infrared Spectroscopy (FTIR).....	37
3.3.5	Photoluminescence Spectra (PL) .....	37
3.4	RESULTS.....	37
3.4.1	Morphological, Chemical and Optical Properties of NWs.....	37
3.4.2	Localized Surface Plasmon Resonance.....	39
4.	CONCLUSIONS AND FUTURE RECOMMENDATIONS .....	45
4.1	CONCLUSIONS .....	45
4.2	FUTURE RECOMMENDATIONS.....	46
	REFERENCES .....	47

## LIST OF FIGURES

### FIGURES

- Figure 1.1.1:** Schematics of the classification of nanomaterials according to their dimensions; (a) 0D (QDs), (b) 1D (nanowires), (c) 2D (thin films) and (d) 3D (nanoparticles) ..... 1
- Figure 1.1.2:** Particle size dependent melting temperature of (a) Au, (b) Cu and (c) Si ..... 2
- Figure 1.1.3:** Coulomb diamonds formed due to the coulomb blockade with different applied voltages ..... 3
- Figure 1.1.4:** Color variation of the emitted lights from quantum dots (QDs) depending on particle size. Wavelength of the emitted light redshifts with particle size. (b) Corresponding emission spectra of the QDs ..... 3
- Figure 1.1.5:** Current flow between two ferromagnetic films that are aligned (a) parallel and (b) anti-parallel ..... 4
- Figure 1.1.6:** SEM images of (a) metallic Ag NWs, (b) semiconducting ZnO NWs and (c) Si NWs ..... 5
- Figure 1.2.1:** Schematic illustration for the synthesis of Si NWs via VLS method ..... 6
- Figure 1.2.2:** Schematic model explaining the SFLS method. The supercritical fluid first dissolves into a metal catalyst (nanocrystal), then nucleation and growth of NW occurs ..... 7
- Figure 1.2.3:** SEM images showing (a) nanosphere lithography for the production of an etching mask, (b) produced etch mask from Cr and (c) morphological variation of fabricated Si NWs with etching time ..... 8
- Figure 1.2.4:** Schematics for the evolution of vertical arrays of Si NWs in MAE process from cross sectional and top views. Ag nanoparticles catalyze etching of the underneath silicon. At the end of the process, vertical arrays of Si NWs were formed ..... 9
- Figure 1.2.5:** Effect of solution concentration on the evolution of decent Si NWs a) 0.01 M AgNO<sub>3</sub>/4.6 M HF, b) 0.02 M AgNO<sub>3</sub>/7.0 M HF, c) 0.04 M AgNO<sub>3</sub>/4.6 M HF and d) 0.02 M AgNO<sub>3</sub>/4.6 M HF. Scales are the same and correspond to 10 μm ..... 10
- Figure 1.2.6:** Effect of solution temperature on NW length in MAE process. Etching time was fixed to 60 minute and solution concentration of 0.02 M AgNO<sub>3</sub>/4.6 M HF was used. 11
- Figure 1.2.7:** Effect of etching time on NW length in MAE process; (a) 20, (b) 60, (c) 100 and (d) 210 minute. Etching temperature was fixed to room temperature and solution concentration of 0.02 M AgNO<sub>3</sub>/4.6 M HF was used ..... 11

<b>Figure 1.3.1:</b> (a) Schematic of single p-Si NW FETs and SEM image of the NW in contact with electrodes, (b) effect of thermal annealing on the I-V behavior of the device and contact resistance and (c) effect of surface passivation of the NWs on the transconductance and mobility.....	13
<b>Figure 1.3.2:</b> Fabrication schematics of Si NWs based thin film composite FETs, SEM image of NWs in contact with electrodes, photograph of bended device and its FET characteristics.....	14
<b>Figure 1.3.3:</b> Reflectivity of bare Si and Si NWs showing the excellent light trapping ability of NW textured surfaces.....	15
<b>Figure 1.3.4:</b> (a) Representative schematic of fabricated heterojunction solar cells and sketches of radial and planar junction, comparison of radial and planar junction solar cells in terms of (b) external quantum efficiency and (c) current density-voltage characteristics and (d) photovoltaic conversion efficiencies with different NW lengths.....	16
<b>Figure 1.3.5:</b> (a) Photographs of industrial size ARC coated and NW textured solar cells and SEM image of NWs in contact with top electrode. Electrical characterizations of ARC coated and NW textured solar cells for (b) photovoltaic conversion efficiencies, (c) external quantum efficiencies and (d) current density-voltage characteristics with different NW lengths.....	17
<b>Figure 2.1.1:</b> Schematics of different NW integration routes using direct growth; (a) single, (b) multiple ordered, (c) multiple random in plane, (d) multiple random out of plane, (e) vertical ordered and (f) vertical random.....	20
<b>Figure 2.1.2:</b> Schematics of different NW integration routes for transfer printing or pick and place; (a) ordered 2D to 2D, (b) random 3D to 2D, (c) ordered 3D to 2D and (d) ordered 3D to 3D.....	21
<b>Figure 2.1.3:</b> Schematics of (a) axial junction and (b) core-shell radial junction photodiode architectures.....	22
<b>Figure 2.1.4:</b> Schematic structure of a MSM photodetector. Bias is applied through metal contacts in between photoactive region (NWs) is placed.....	23
<b>Figure 2.1.5:</b> SEM image of vertical arrays of Si NWs used in photodetector applications. (a) MIS photodetector, (b) MSM photodetector. Scale bar corresponds to 500 nm.....	23
<b>Figure 2.1.6:</b> SEM images of planar Si NW arrays in photodetector applications.....	24
<b>Figure 2.4.1:</b> (a) A photograph of Si wafer with Si NW arrays, SEM image of vertically aligned Si NWs and Si NWs dispersed in water. (b) Photographs of the vacuum filtration setup, Si NW networks on filtration membrane and on glass.....	27

<b>Figure 2.4.2:</b> SEM images of Si NW networks with different densities of (a) 0.87, (b) 1.87 and (c) 3.44 NWs / $\mu\text{m}^2$ . (d) Transmittance spectrum of the NW networks with different NW densities. Transmittance of Ag NW network was provided for comparison.....	28
<b>Figure 2.4.3:</b> (a) SEM image of the MSM structure. Inset shows that the channel gap was free from Ag NW prior to Si NWs transfer. (b) Representative device architecture and (c) photograph of the final device and scale bar corresponds to 2.5 cm.....	29
<b>Figure 2.4.4:</b> (a) Photoresponsivities with different NW densities under a 10 V bias. (b) I-V characteristics of the device (1.87 NWs/ $\mu\text{m}^2$ ). Inset is the logarithmic plot. (c) Light ON-OFF measurements with different NW densities under 5 V bias and (d) dynamic response behavior (1.87 NWs/ $\mu\text{m}^2$ ) under a 5 V bias.....	30
<b>Figure 2.4.5:</b> (a) Light ON-OFF measurements under 5 V bias showing that the device is operational upon bending. (b) I-V characteristics of the bent device. (c) Dark/light currents under a bias of 5 V showing stability of the devices in the investigated range. (d) Photograph of a flexible device at a bending radius of 1 cm. A NW density of 1.87 NW/ $\mu\text{m}^2$ was used for flexible devices.....	32
<b>Figure 3.1.1:</b> Light-metal nanoparticle interaction, (a) scattering of light by far-field effect and (b) enhancement of electromagnetic field close to the metal nanoparticle by near-field effect.....	33
<b>Figure 3.1.2:</b> Relative motion of free electrons with the incident electromagnetic field in the resonance condition.....	34
<b>Figure 3.4.1:</b> TEM images of (a) one-step and (b) two-step etched Si NW showing surface morphologies. (c) FTIR spectrum of one-step and two-step etched Si NWs. (d) PL spectrum from two-step etched NWs.....	38
<b>Figure 3.4.2:</b> Evolution of discrete and spherical Ag nanoparticles upon annealing. Cross-sectional SEM images of (a) as evaporated and (b) annealed Si NWs. Both scales are the same.....	39
<b>Figure 3.4.3:</b> Top-view SEM images of Ag nanoparticle decorated two-step etched Si nanowires with different Ag thicknesses of (a) 12 nm, (b) 24 nm and (c) 36 nm. (d) Top-view SEM image of Ag nanoparticle decorated one-step etched Si nanowires with Ag thicknesses of 36 nm. All scales are the same. Inset shows the 3 $\mu\text{m}$ long vertical arrays of Si NWs fabricated with two-step etching. Inset scale corresponds to 5 $\mu\text{m}$ .....	41
<b>Figure 3.4.4:</b> (a) Diffuse reflectance spectrum for 12, 24 and 36 nm Ag deposited samples that are (a) 3 $\mu\text{m}$ long one-step etched Si nanowires and (b) their corresponding spectral enhancement ratios. (c) Diffuse reflectance spectrum for 3 $\mu\text{m}$ long two-step etched Si nanowires and (d) their corresponding spectral enhancement ratios.....	42
<b>Figure 3.4.5:</b> Photographs of one-step (below) and two-step (above) etched Si NWs with different Ag thicknesses.....	43

**Figure 3.4.6:** (a) Diffuse reflectance spectra for 24 nm thick Ag deposited 3, 5 and 10  $\mu\text{m}$  long Si NWs. Dashed lines indicate the bare NW. (b) Corresponding spectral enhancement ratios.....43

## CHAPTER 1

### INTRODUCTION

#### 1.1 FEATURES OF NANOMATERIALS

The concept of nanotechnology was first disclosed by the lecture entitled, “There is plenty of room at the bottom”, given by famous physicist Richard Feynman in 1959 at Caltech USA. Some of the presented ideas have been accomplished; but, some have not. For instance fabrication of functional nanomaterials has been discovered only in the last decades. Nanomaterials are in atomic or molecular level and their sizes are within the range of 1-100 nm. Compared to the bulk materials, nanomaterials have enormously high surface to volume ratio. Moreover, there are too many unbounded atoms at their surface. Hence, they exhibit unique electrical, thermal, magnetic, optical and mechanical properties. There are 4 types of nanomaterials according to their dimensionality, as shown in Figure 1.1.1. Quantum dots (QDs) are classified as zero dimensional (0D), nanowires, nanotubes, nanorods and nanobelts as one dimensional (1D), thin films as two dimensional (2D) and nanoparticles are classified as three dimensional (3D) nanomaterials.

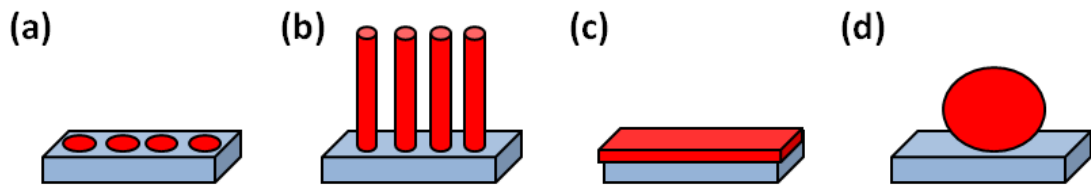


**Figure 1.1.1:** Schematics of the classification of nanomaterials according to their dimensions; (a) 0D (QDs), (b) 1D (nanowires), (c) 2D (thin films) and (d) 3D (nanoparticles).

##### 1.1.1 Thermal, Electrical, Optical and Magnetic Properties of Nanomaterials

One of the surprising properties of nanomaterials is their thermal behaviour. When melting point of a material is considered, it is evident that it can be directly correlated to the bond strength. In bulk systems, surface to volume ratio is small and the surface curvature effect can be neglected. Decreasing the size to nanometer scale; however, drastically increases surface to volume ratio. Moreover; the surface curvature effect becomes more dominant. These two parameters decrease the melting temperature of the nanomaterial leading to a size dependent melting point. Size dependency of melting temperatures for gold (Au), copper (Cu) and silicon (Si) are given in Figure 1.1.2.

Another interesting point is the electrical properties of nanomaterials. Decreasing the size of the material creates distinct energy levels in the energy band diagram. In fact, playing with the size can change the behavior of materials being from metallic to semiconductor or to an insulator in extreme cases. Size reduction in materials causes two different effects in terms of electrical properties. First one is the separation of energy levels from each other creating quantum confinement effect. Quantum effect is confining charge carriers in an area small enough that their wave-like behavior dominates over particle like behavior. Second one is the classical effect in which the size of the system approaches the mean free path of inelastic scattering of electrons. In this case, drastic decreases in the scattering events occur. For 0D and 1D nanomaterials, an interesting phenomenon may take place between distinct energy levels, called electron tunneling. This is simply the penetration of the electrons through a potential barrier although it does not have enough energy to overcome. This phenomenon can be used to build single electron transistors and quantum computers. The requirement behind the quantum computing is using QDs, where individual electrons can tunnel through upon application of a bias voltage between electrodes that are connected to the quantum dot. Following tunneling, individual electrons could stay within the dot for a distinct period of time. Since the energy levels for electron occupancy are limited, another electron is prevented from tunneling causing Coulomb Blockade. Figure 1.1.3 shows the coulomb diamonds. Inside the diamond's area, there is no electron tunneling to the QD due to Coulomb Blockade and it can be manipulated by adjusting applied potential between electrodes and to the QD.

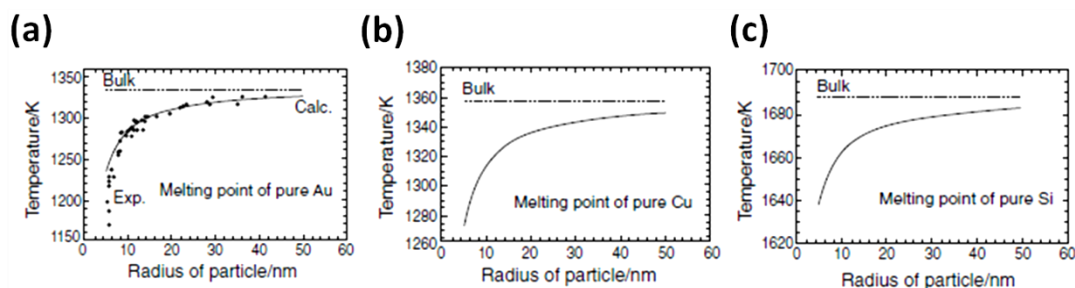


**Figure 1.1.2:** Particle size dependent melting temperature of (a) Au, (b) Cu and (c) Si [1].

Nanomaterials also have interesting optical properties. Absorption and emission of photons depend on the energy difference between valence and conduction band edges of the materials and tuning these properties by particle size is possible. As the size decreases, the band gap of material increases. This widening of the band gap may alter the absorption characteristics of the matter turning an opaque material to transparent. Same phenomenon can be observed for light emission. Since the band gap can be tuned by the particle size, wavelength of the emitted light from luminescent materials can be changed. Figure 1.1.4 shows the particle size

dependent color variation of the emitted light from colloidal QDs. An increase in the particle size redshifts the wavelength of the emitted light.

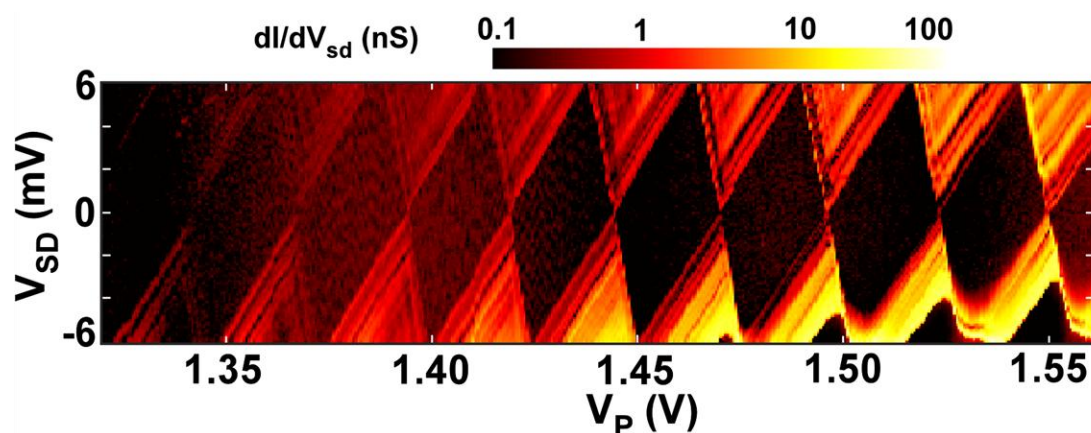


**Figure 1.1.3:** Coulomb diamonds formed due to the Coulomb Blockade with different applied voltages [2].

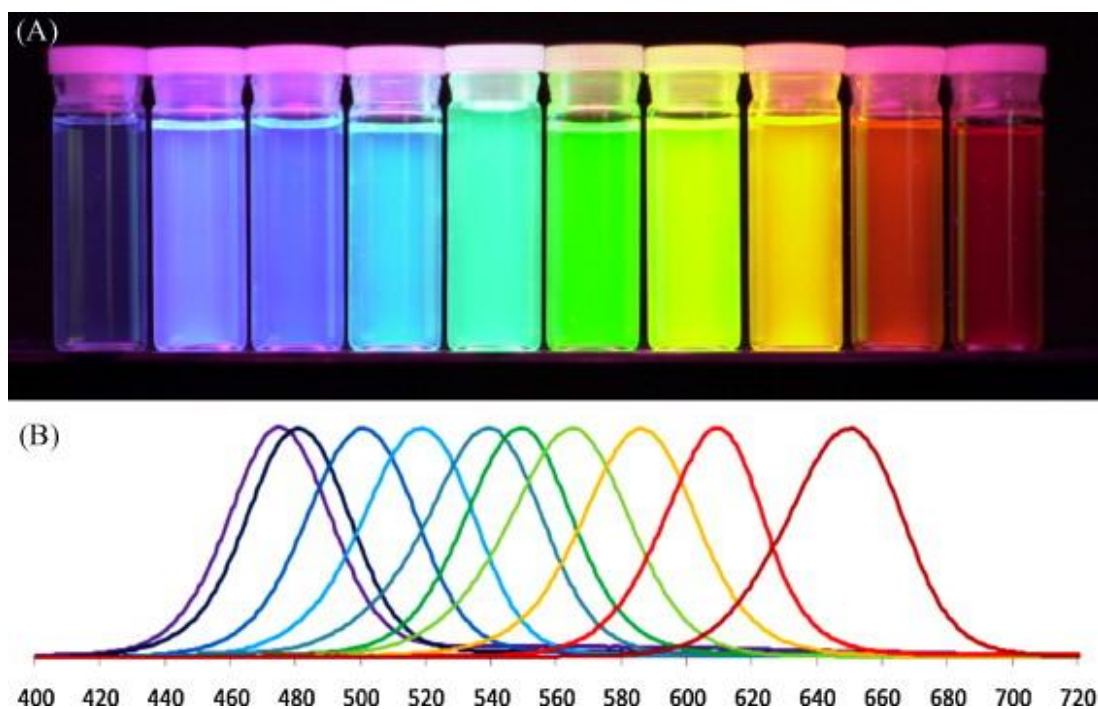


**Figure 1.1.4:** Color variation of the emitted lights from QDs depending on particle size. Wavelength of the emitted light redshifts with particle size. (b) Corresponding emission spectra of the QDs [3].

For the case of magnetic properties, the most prominent effect of nanomaterials might be giant magnetoresistance (GMR). The principle behind this phenomenon is the resistance between two different ferromagnets and different spin states (spin up or spin down). In this case, conduction depends on the magnetization being whether parallel or anti-parallel. Parallel condition would allow electrons with certain spin states (up or down) to pass through leading to a net current (Figure 1.1.5 (a)). On the other hand, anti-parallel magnetization would not create any current between two ferromagnets (Figure 1.1.5 (b)). The main application of this effect is magnetic field sensors. They are used to read data from the hard disk drives. They can also be used for magnetic data storage as in the case of magnetoresistive random-access memory (MRAM).

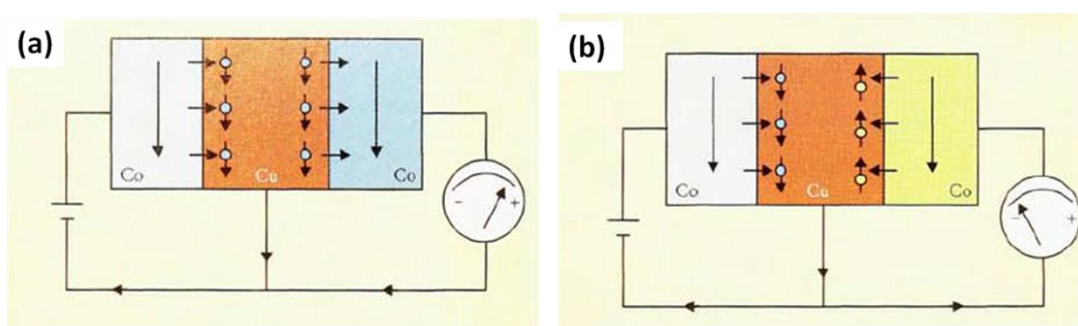


**Figure 1.1.5:** Current flow between two ferromagnetic films that are aligned (a) parallel and (b) anti-parallel [4].

### 1.1.2 Nanowires as 1D Nanomaterials

Combination of quantum confinement with improved electrical transport and increased surface area, 1D nanomaterials show unique properties, which open up new application areas compared to their bulk counterparts.

Nanowires can be further categorized in three groups according to their electrical properties, namely metallic (i.e. Ag and Cu NWs), semiconducting (i.e. ZnO and Si NWs) and insulating (i.e. SiO<sub>2</sub> and TiO<sub>2</sub> NWs). Scanning electron microscope (SEM) images of Ag, ZnO and Si NWs are provided in Figure 1.1.6. All of these may become functional units for electronic, optoelectronic and electromechanical devices. Large scale synthesis and assembly of these nanowires with controlled morphology, dimensions, purity and composition is crucial for their utilization in these devices.

Semiconducting NWs have received special interest among others due to low electron density, efficient charge transport and low effective mass [5, 6]. Si NWs may be the most important semiconducting nanowires since Si in bulk form is the building block for optoelectronic and microelectronic industry [7, 8]. Si industries R&D investments are around 45 \$ billion per year [9]. Almost 50 years of effort has been spent on the evolution of Si

technology. Hence, shifting this level of knowledge and capital onto another material is not affordable. Being the key component of the semiconductor industry, Si in the NW form has become one of the most emerging 1D nanomaterial.

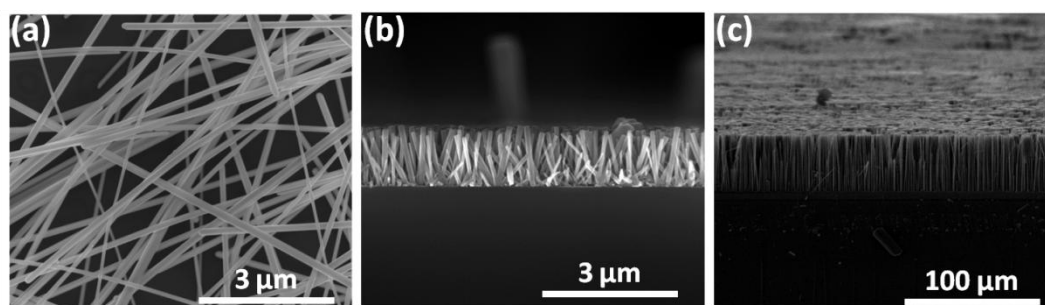


**Figure 1.1.6:** SEM images of (a) metallic Ag NWs, (b) semiconducting ZnO NWs and (c) Si NWs.

## 1.2 FABRICATION OF Si NWS

Si NWs can be fabricated by two approaches. First one is the bottom-up approaches. This method can be regarded as building up of a nanomaterial starting from its building blocks, atoms. Some of the bottom-up approaches are vapor-liquid-solid (VLS) [10], molecular beam epitaxy (MBE) [11], supercritical fluid liquid solid (SFLS) [12] and laser ablation methods [13]. Second one is the top-down approaches. Within these, a bulk material is carved down to get nano-size materials. Some of the top-down approaches include lithographical methods [14], deep reactive ion etching (DRIE) [15] and most recently introduced, metal-assisted-chemical etching (MAE) method [16-19].

### 1.2.1 Bottom-Up Approach for the Fabrication of Si NWs

#### 1.2.1.1 Vapor-Liquid-Solid (VLS) Method

VLS method is one of the most common bottom-up method for the fabrication of Si NWs. It is first proposed by Wagner and Ellis in 1964 [10]. It necessitates a metal catalyst and a vapor source. Furthermore, NW material to be synthesized should form a eutectic phase within the metal catalyst used. For the synthesis of Si NWs, gold (Au) is used as metal catalyst and silane ( $\text{SiH}_4$ ) or silicon tetrachloride ( $\text{SiCl}_4$ ) gases are used as silicon precursors.

A representative sketch for the growth of Si NWs through VLS and Au-Si phase diagram are provided in Figure 1.2.1. A very thin layer Au is deposited on growth substrate. At a certain temperature, Au film divides into droplets and reacts with Si feedstock and forms Au-Si eutectic alloy. Then, Si starts to dissolve in the droplet and after the supersaturation point, Si nucleates beneath the droplet. From this point, supersaturation and growth of Si NW occurs

simultaneously. The fabricated NW diameter is defined with the size of Au-Si droplet. Although it allows fabrication of high purity NWs, the Au cap remains at the top and may cause some problems for device applications. Additionally, this method requires controlled atmosphere to prevent oxidation of the NWs and necessitate the use of hazardous precursors (i.e.  $\text{SiH}_4$  and  $\text{SiCl}_4$ ) and relatively high temperature ( $\sim 900$  °C). In addition, synthesis of Si NWs over large areas is trivial due to the system and vacuum limitations.

### 1.2.1.2 Super Critical-Fluid-Liquid-Solid (SFLS)

This method is similar to the VLS method. However, instead of growing wires in a vacuum environment, SFLS method uses a solution phase. SFLS necessitates supercritical fluids of precursors at high temperatures and a metal catalyst like Au. Au nanocrystals define the diameter and the orientation of the NWs. They have been isolated from each other with organic surfactants. Since most of the organic ligands boil at high temperature, pressure is needed to catalyze the growth. At high temperature and pressures, supercritical fluid starts to decompose forming the precursor of the intended NW. From this point, supersaturation, nucleation and the growth of the NW occurs as in the case of VLS method. The schematic of SFLS method is given in Figure 1.2.2.

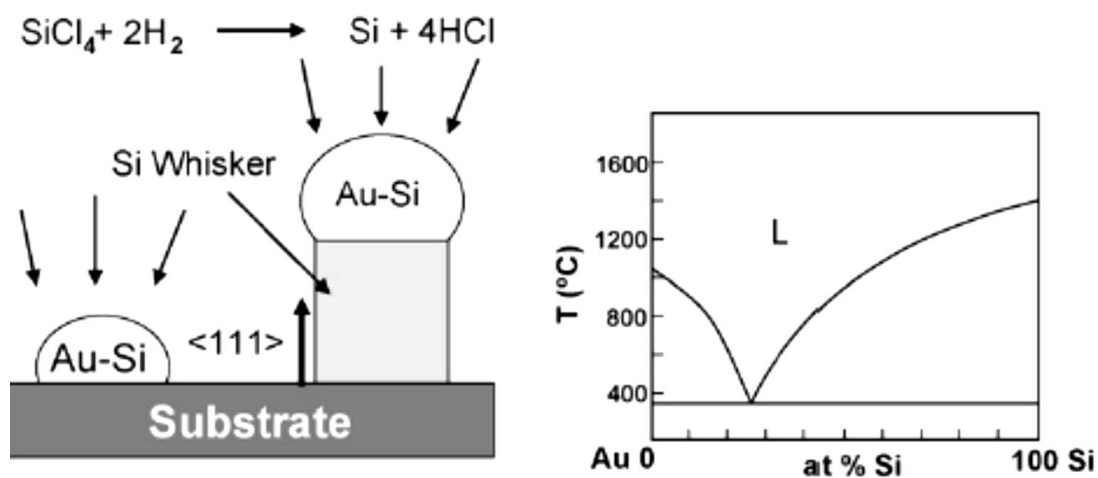


**Figure 1.2.1:** Schematic illustration for the synthesis of Si NWs via VLS method and Au-Si phase diagram [20].

This method has higher yield than VLS, since the solution phase has higher precursor solubility compared to the vapor phase. Moreover, this method allows the fabrication of single-crystal, defect free NWs close to the diameters of metal catalyst. The presence of organic ligands prevents agglomeration of crystals. Hence, control over the diameter of the NW is higher than the VLS method.

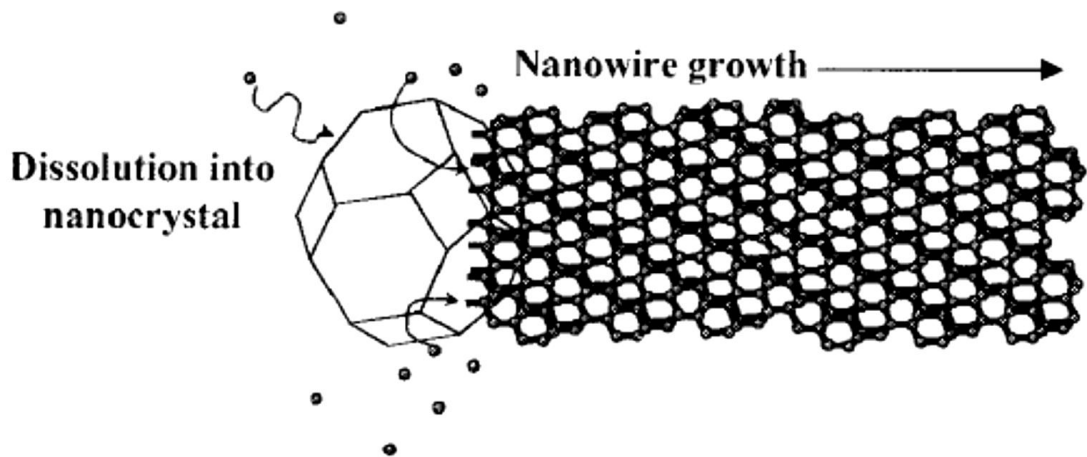


**Figure 1.2.2:** Schematic model explaining the SFLS method. The supercritical fluid first dissolves into a metal catalyst (nanocrystal), then nucleation and growth of NW occurs [12].

## 1.2.2 Top-Down Methods For the Fabrication of Si NWs

### 1.2.2.1 Deep Reactive Ion Etching (DRIE)

This method is utilized for the production of high aspect ratio features using anisotropic etching. It consists of several steps for the fabrication of Si NWs. The first step is defining the diameter of the NWs with an etching mask. The mask prevents the etching of the substrate underneath so that the diameter of the Si NWs can be determined. In this manner, lithographical methods are used. Nanosphere lithography, electron beam lithography and nanoimprint lithograph are widely used for this purpose. Figure 1.2.3 (a) and (b) shows the SEM images of the nanospheres deposited onto substrate for defining the etch mask and produced etch masks following chromium (Cr) deposition, respectively. After creating the lithographical features, plasma etching takes place. Etching includes two different reactive chemicals. First one is sulfur hexafluoride/dioxide ( $\text{SF}_6/\text{O}_2$ ) mixture.  $\text{SF}_6/\text{O}_2$  etches substrate isotropically. However, the second chemical, octafluorocyclobutane ( $\text{C}_4\text{F}_8$ ), passivate the sidewalls and prevents lateral etching. These two chemicals are sequentially bombarded onto the substrate. After hundreds of etching and passivation steps, anisotropic etching occurs yielding high aspect ratio Si NWs as shown in the SEM images provided in Figure 1.2.3 (c).

### 1.2.2.2 Fabrication of Si NWs Through MAE Method

Bottom-up methods usually necessitate complex equipment, high temperatures, vacuum and hazardous Si precursors, all of which drastically increase the cost of the processes. However, top-down approaches and especially the MAE method allows cost effective fabrication. It is first proposed by Peng et al. [17] and widely used since then. It is because it offers a powerful, simple and solution-based process. It allows the fabrication of Si NW arrays over large areas without patterning prior to the etching process. By the nature of the process, the resulting Si NWs inherit the starting wafer characteristics, such as the doping type, density, conductivity and crystal orientation [6].

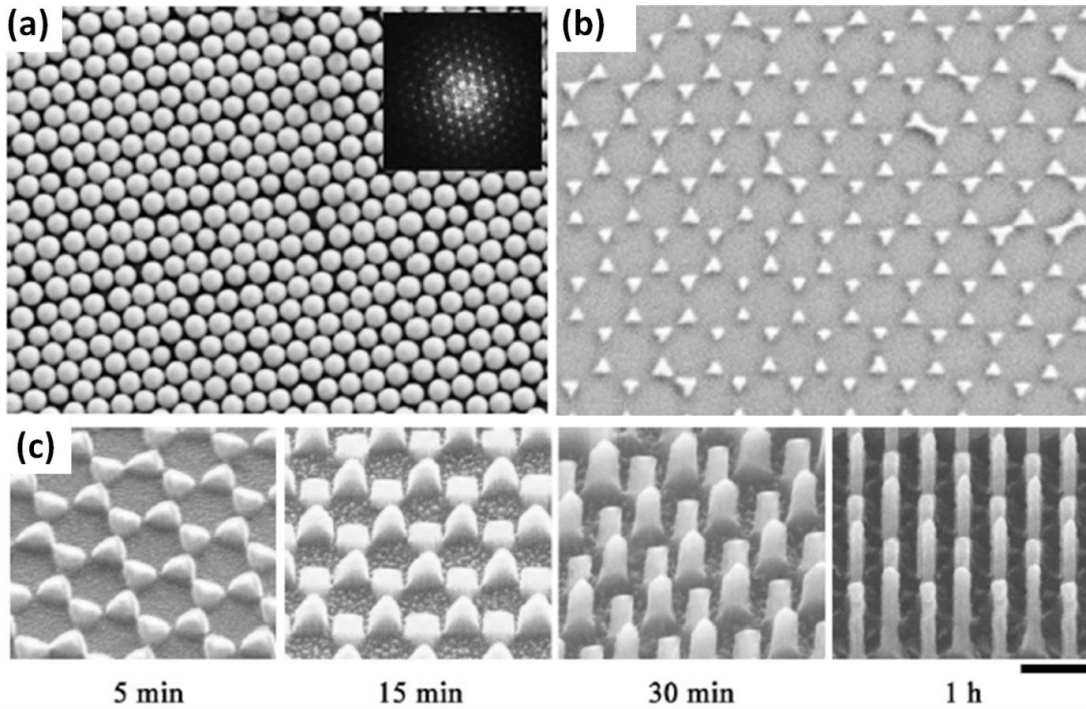
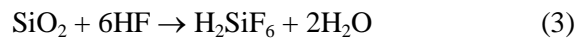
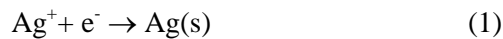


**Figure 1.2.3:** SEM images showing (a) nanosphere lithography for the production of an etching mask, (b) produced etch mask from Cr and (c) morphological variation of fabricated Si NWs with etching time [21].

In this method, etching of Si occurs in aqueous solution containing Ag ions ( $\text{Ag}^+$ ) and hydrofluoric acid (HF). This method can be summarized into cathodic reduction of Ag ions, anodic oxidation and dissolution of Si taking place underneath the Ag deposits. The electron transfer between Si and Ag occurs within energetically favorable crystallographic orientations yielding to an anisotropic etching.



The proposed mechanism for the MAE method is as follows. Through the immersion of Si wafer into  $\text{AgNO}_3/\text{HF}$  solution, Ag ions capture electrons from the valence band of Si and form Ag nanoparticles. Since heterogeneous nucleation necessitates lower energy compared to homogeneous counterpart, Ag nanoparticles easily form near the defects of Si. Due to the different electronegativities, Ag nanoparticle attracts electrons from Si and become negatively charged. Hence, negatively charged nanoparticles catalyze the further nucleation of Ag ions. As a result of this, Si underneath Ag is oxidized. As  $\text{SiO}_2$  forms, HF immediately dissolves and forms etching pits. Hence, Ag nuclei sink toward Si. The schematics

explaining mechanism of MAE are given in Figure 1.2.4. These reactions are spontaneous and continue unless stopped, forming vertical arrays of Si NWs.

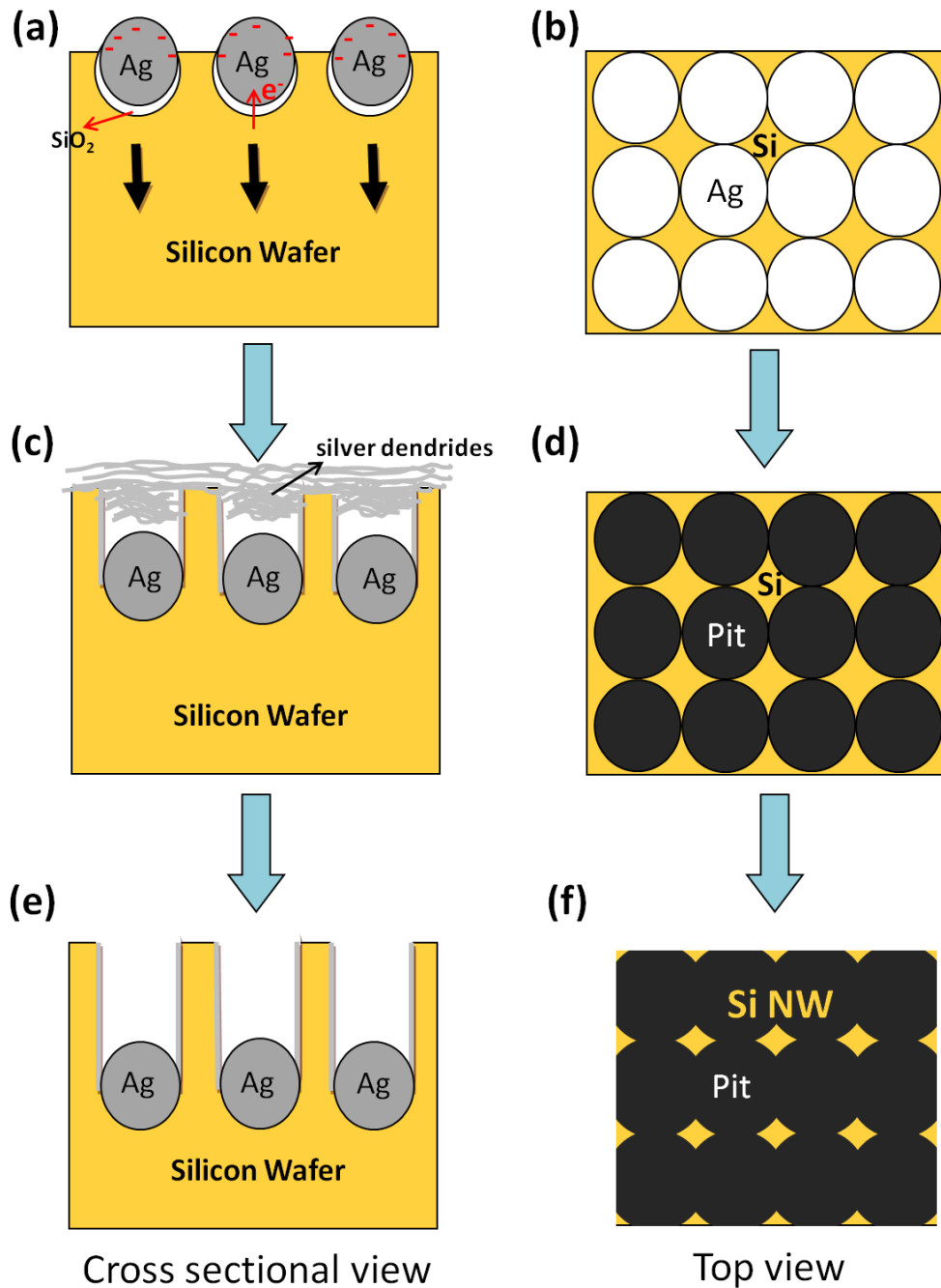


**Figure 1.2.4:** Schematics for the evolution of vertical arrays of Si NWs in MAE process from cross-sectional and top views. Ag nanoparticles catalyze etching of the underlying Si. At the end of the process, vertical arrays of Si NWs were formed [26].

There are some important parameters in this technique. Since oxidation and dissolution are competitive reactions, solution concentration might be the most important parameter for obtaining decent NWs. There are many efforts for the investigation of the optimum solution concentration and optimum concentration is reported as the mixture of 0.02 M  $\text{AgNO}_3$  and 4.6 M HF [17-19, 22-25]. Figure 1.2.5 shows the cross sectional SEM images of NWs fabricated at different solution concentrations. As it can be seen from SEM images, vertical arrays of Si NWs forms when the solution concentration reaches to mixture of 0.02 M  $\text{AgNO}_3$  and 4.6 M HF [26]. The other important parameters are solution temperature and etching time. Cross sectional SEM images of Si NWs fabricated changing solution temperature and etching time are provided in Figure 1.2.6 and Figure 1.2.7, respectively. NW length was found to be linearly dependent on both parameters.

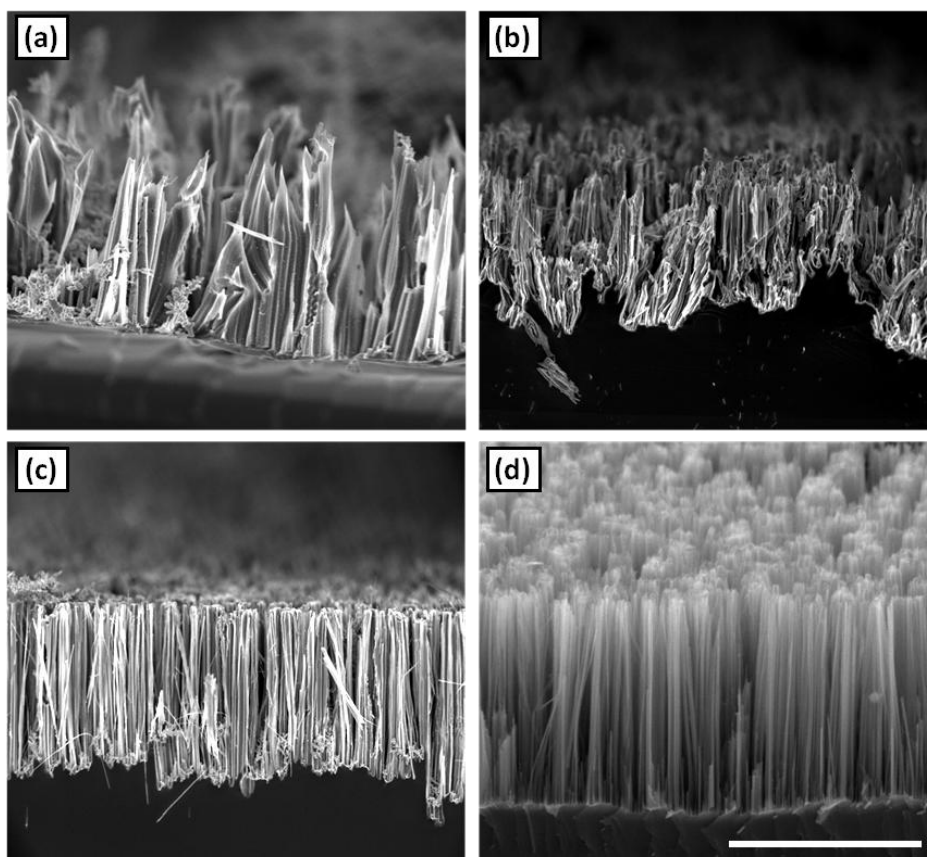


**Figure 1.2.5:** Effect of solution concentration on the evolution of decent Si NWs; a) 0.01 M  $\text{AgNO}_3$ /4.6 M HF, b) 0.02 M  $\text{AgNO}_3$ /7.0 M HF, c) 0.04 M  $\text{AgNO}_3$ /4.6 M HF and d) 0.02 M  $\text{AgNO}_3$ /4.6 M HF. Scales are the same and corresponds to 10  $\mu\text{m}$  [26].

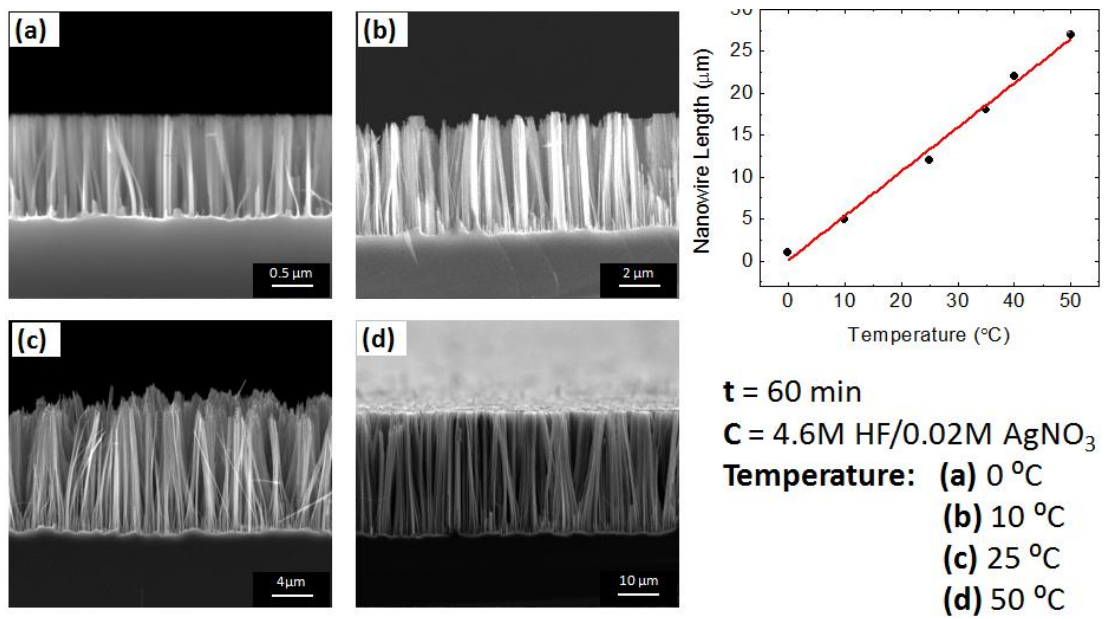


**Figure 1.2.6:** Effect of solution temperature on NW length in MAE process. Etching time was fixed to 60 minutes and a solution concentration of 0.02 M AgNO<sub>3</sub>/4.6 M HF was used [19].

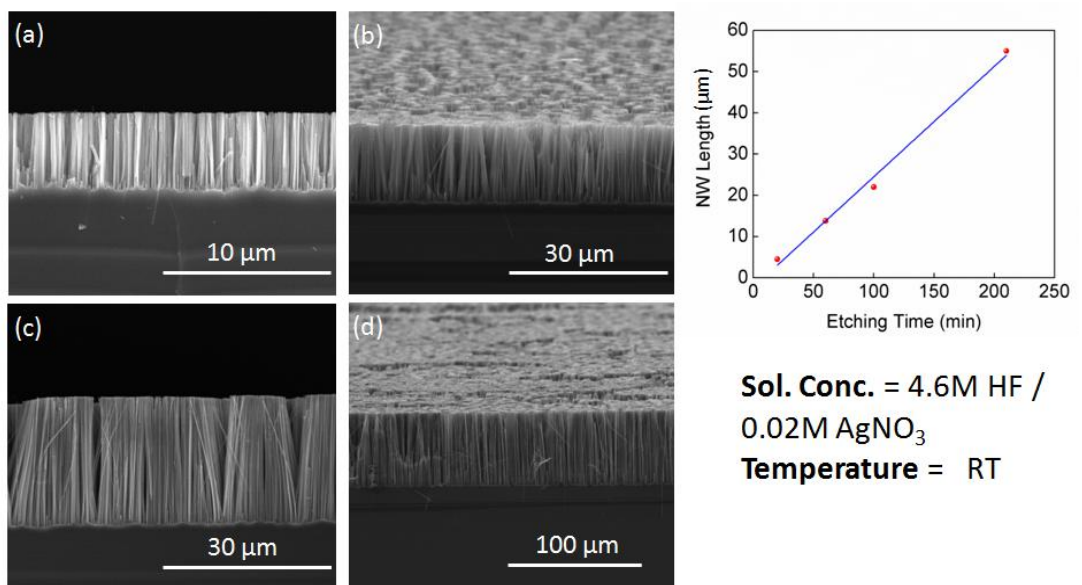


**Figure 1.2.7:** Effect of etching time on NW length in MAE process; (a) 20, (b) 60, (c) 100 and (d) 210 minute. Etching temperature was fixed to room temperature and solution concentration of 0.02 M AgNO<sub>3</sub>/4.6 M HF was used.

### 1.3 EMERGING APPLICATIONS OF Si NWS

Si NWs have been used in a wide range of prototype applications, where they offer new functional properties for future technology. These applications can be listed as solar cells [22, 24, 25, 27-33], field effect transistors (FETs) [34, 35], thermoelectric applications [36, 37], lithium batteries [38, 39], light emitting diodes (LEDs) [40] and photodetectors [41-48]. In this chapter, the new insights offered by Si NWs will be covered in detail for FETs and solar cells.

#### 1.3.1 Field Effect Transistors (FETs)

FETs are the key elements for computer technology. Enhancing their performance is a challenge for future computers with higher speed and/or capacity. Adapting NW technology into current FETs might open up new insights for future electronics. In addition, implementing Si NWs into this technology is easier than other semiconducting materials. Deposition of a NW onto an insulating substrate, deposition of contacts to the ends of NWs is the most basic approach for the fabrication of the FETs. This approach allows the creation of nanoscale building blocks that can simply be integrated into a more complex planar circuitry. Initial studies of Si NWs on FETs showed low transport and carrier mobilities [49]. However, further studies done by Cui et al. [50] revealed that surface passivation and contact annealing are the two important parameters for achieving high performance FETs. They have used an individual *p*-type Si NW and defined the electrical contacts (Ti/Au) with electron beam lithography. They found that rapid thermal annealing decrease the contact resistance by almost 260 times. Moreover, they have coated the NWs with 4-nitrophenyl octadecaonate for surface passivation. This chemical allowed a stable and nonpolar Si-O-C linkage leading to passivation. Figure 1.3.1 (a) shows the schematic of the fabricated device, SEM image of a single NW between source and drain electrodes. Figure 1.3.1 (b) and (c) shows the effect of thermal annealing on the contact resistance and effect of surface passivation on the device characteristics, respectively. Green (red) color designates before (after) thermal treatment or surface passivation. Thermal annealing decreases the contact resistance, while surface passivation enhances the transconductance and mobility. Transconductance and mobility of 2000 nS and 1350 cm<sup>2</sup>/Vs obtained, respectively. They have compared the transconductance values with planar Si devices and obtained almost a 10-fold enhancement. Hence, Si NWs have the potential for exceeding the conventional device performance limits and could be ideal building blocks for future electronics.

Another interesting study on FETs were performed by Moon et al. [51]. They have fabricated Si NW thin film composite on the poly (4-vinylphenol) (PVP) layer and obtained flexible high performance FETs. They have fabricated Si NWs through the MAE method. The NW solution was drop casted on glass and then polydimethylsiloxane (PDMS) was used to transfer NWs onto PVP layer. Flexible Si NW based FETs were fabricated by evaporating aluminum (Al) as back gate and gold (Au) as source and drain electrodes. Flexible devices upon a bending radius of 2.5 mm was measured and stable values up to 2000 bending cycles

were obtained. Hence, Si NWs might become building blocks for printable and flexible electronics. PDMS stamping schematics, SEM image of NWs in contact with electrodes, a photograph of bended device and its FET characteristics with different bending radiuses are given in Figure 1.3.2.

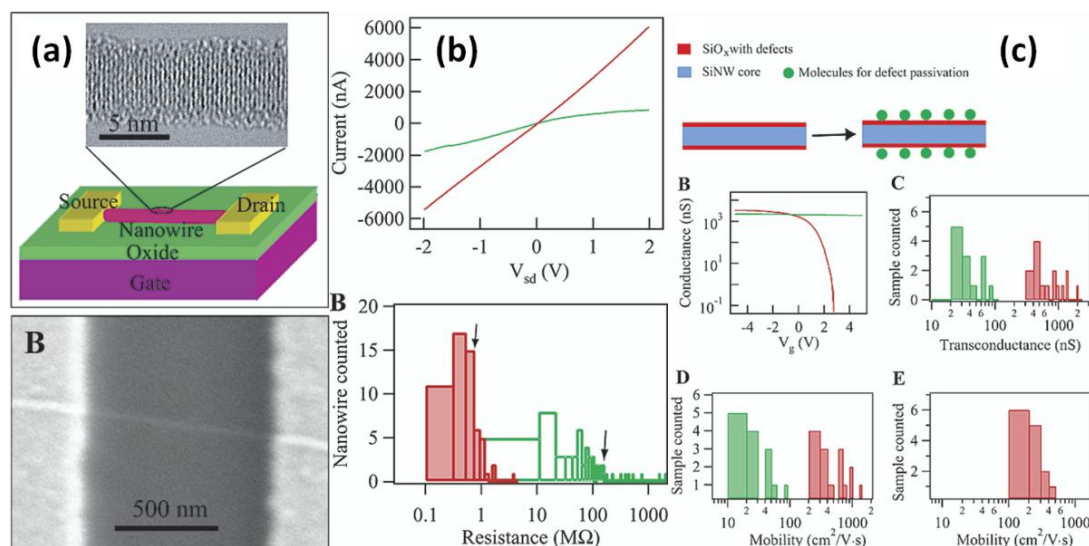


**Figure 1.3.1:** (a) Schematic of a single *p*-Si NW FETs and SEM image of the NW in contact with electrodes, (b) effect of thermal annealing on the I-V behavior of the device and contact resistance and (c) effect of surface passivation of the NWs on the transconductance and mobility [50].

### 1.3.2 Heterojunction Solar Cells

Due to the high carbon dioxide (CO<sub>2</sub>) emission from petroleum based fuels and limited fuel sources all around the world, green and renewable energy sources have been received significant attention in the last decade. In this manner, solar energy is one of the best candidates for the reduction of CO<sub>2</sub> emission. Among the semiconductor family, Si has been widely used for the fabrication of solar cells. Methods and industrial scale processes for the fabrication of Si solar cells were already optimized. However, to decrease the cost of solar modules in terms of watt per dollars, new approaches are needed. There are too many different approaches for this purpose. First one is the use of thinner Si wafers in solar cells [52]. Second one is the use of copper (Cu) top electrode instead of Ag [53]. Cu is cheaper material as compared to Ag and it may help in decreasing the cost of the solar modules. Last one is the introduction of new light trapping mechanisms that could eliminate the need for antireflection coatings (ARCs).

Vertical arrays of Si NWs have enhanced light trapping abilities. Figure 1.3.3 shows the reflectivity of Si NWs compared to bare Si wafer. The enhanced absorption on the NW textured wafer can also be observed by eye (see inset of Figure 1.3.3). Hence, NW textured solar cells do not necessitate the use of ARCs yielding to a decrease in the production cost of solar modules.

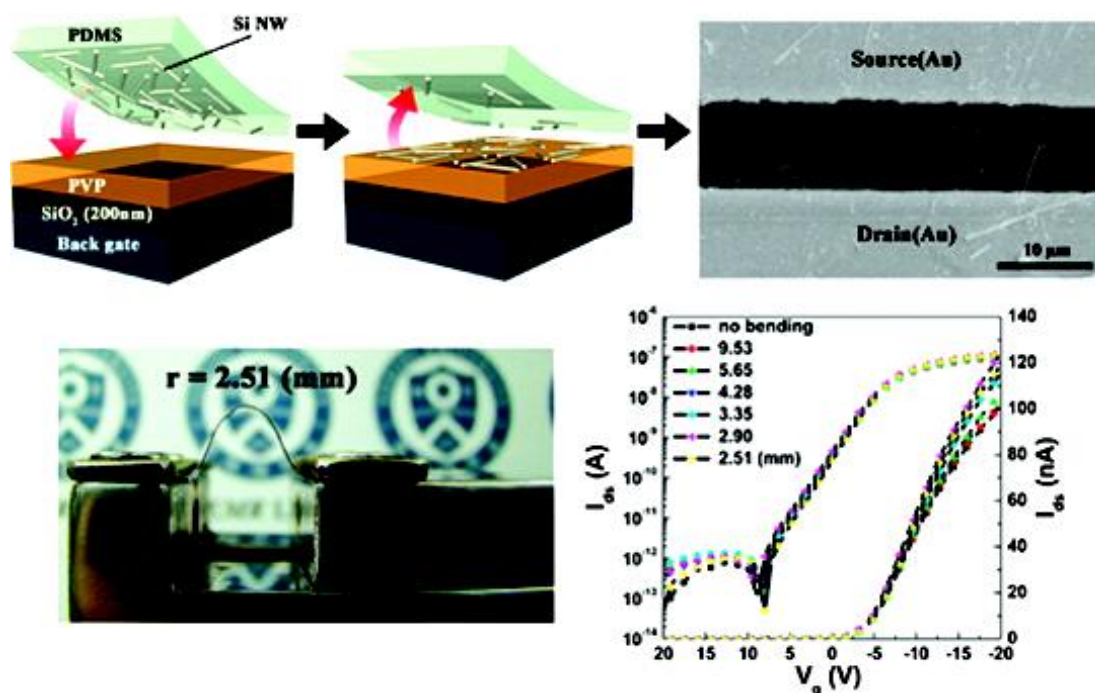


**Figure 1.3.2:** Fabrication schematics of Si NWs based thin film composite FETs, SEM image of NWs in contact with electrodes, photograph of bended device and its FET characteristics [51].

Through the use of vertical arrays of NWs within solar cells, one can obtain radial junctions within the complementary materials instead of a planar junction. Working mechanism of solar cells simply includes the absorption of the incoming photon, generation of electron/hole pairs, their transport and finally collection by the respective electrodes. Radial junction decreases the carrier diffusion length, yielding to enhanced collection and thus solar conversion efficiencies. Figure 1.3.4 (a) shows the schematic structure of planar and radial junctions. Investigation of radial junction for organic-inorganic heterojunction solar cells has been done by Ozdemir et al. [25]. The schematic of the fabricated solar cell is also provided in Figure 1.3.4 (a). Their results are summarized in Figure 1.3.4 (b)-(d). In Figure 1.3.4 (b), increased quantum efficiencies were obtained for radial junction solar cells. This is, in fact, related with the enhanced collection due to the decreased diffusion length of minority

carriers. Furthermore, a similar increase in the current density was obtained, which is also related with the enhanced collection of charge carriers as shown in Figure 1.3.4 (c).

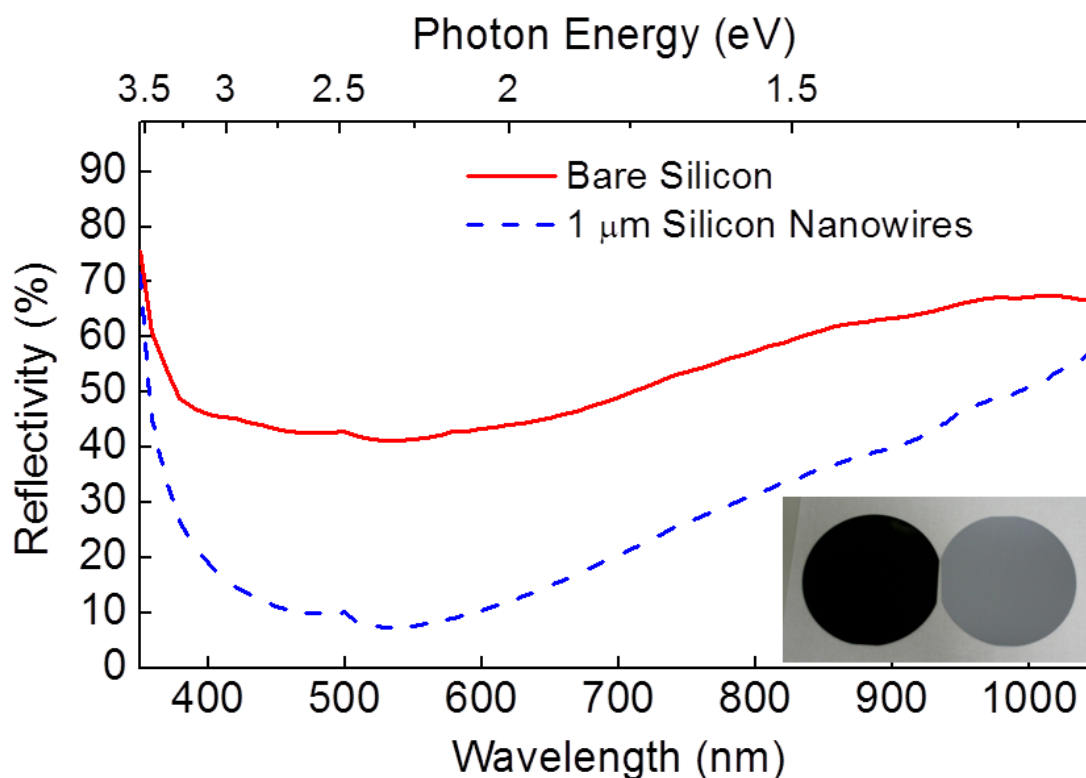


**Figure 1.3.3:** Reflectivity of bare Si and Si NWs, showing the excellent light trapping ability of NW textured surfaces [25].

The current-voltage characteristics of solar cells with different NW lengths are provided in Figure 1.3.4 (d). There was almost a 9-fold increase in the efficiency for the shortest NWs compared to planar wafer. However, this enhancement got lost through the increase in NW length. This was correlated to the carrier entrapment at the surface of the NWs. The MAE process was used for the fabrication of vertical arrays of NWs. Etching nature of the MAE process somehow yields rough surface features for the NWs. The rough surface acts as trapping centers for the charge carriers, enhancing recombination, leading a decrease in the solar conversion efficiency for increased NW length. Similar behavior was obtained in a study by Kulakci et al. [24]. In that particular work, industrial size multicrystalline homojunction solar cells were fabricated with Si NWs and their optoelectronic properties were compared to that of conventional ARC textured Si solar cells. Photographs of the fabricated solar cells are given in Figure 1.3.5 (a). Figure 1.3.5 (b)-(d) shows the effect of NW length on photovoltaic conversion efficiency, external quantum efficiency and current density-voltage characteristics of the devices, respectively. Competitive efficiency values for

the shortest NWs were obtained. Longer NWs were found to deteriorate the efficiency of the solar cells. Although, NWs offered superior properties compared to planar solar cells, surface passivation was recommended as a future work for the stabilization of the cell performances.

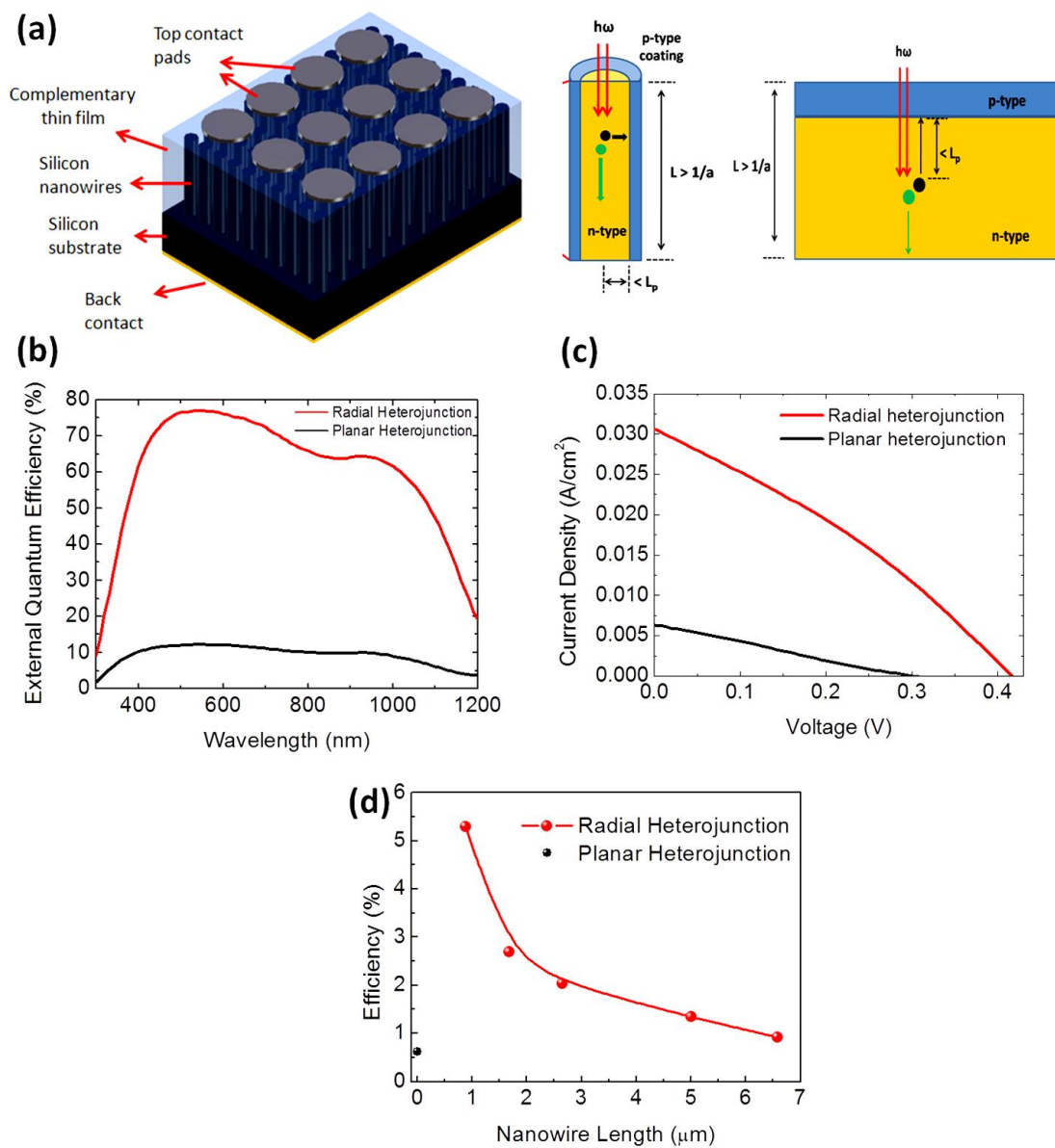


**Figure 1.3.4:** (a) A representative schematic of the fabricated heterojunction solar cells and sketches of radial and planar junction, comparison of radial and planar junction solar cells in terms of (b) external quantum efficiency and (c) current density-voltage characteristics and (d) photovoltaic conversion efficiencies with different NW lengths [25].

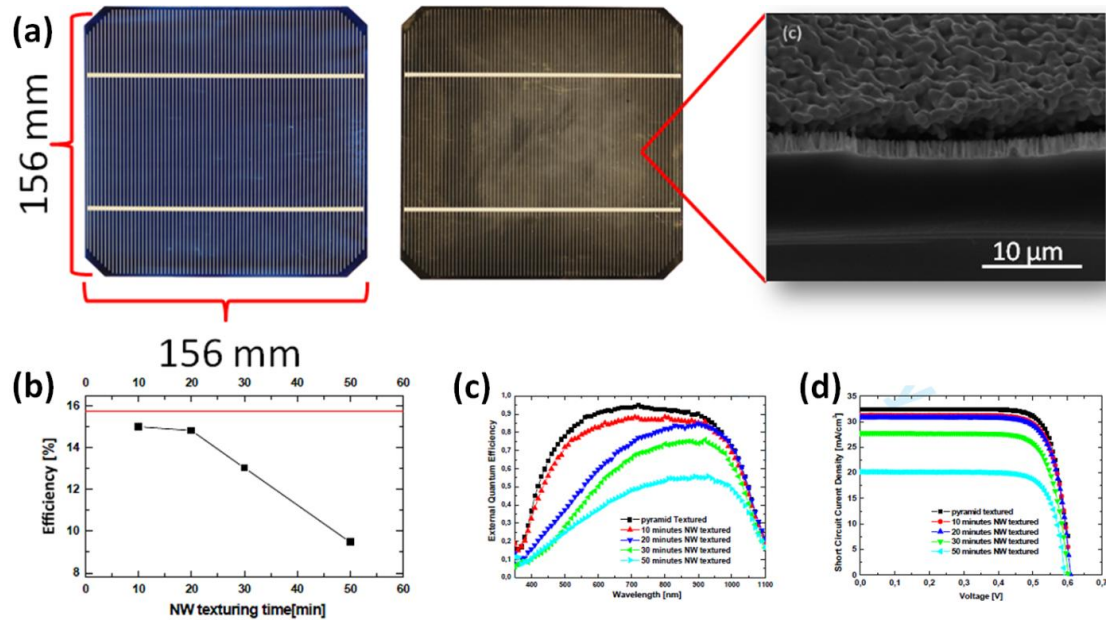


**Figure 1.3.5:** (a) Photographs of industrial size ARC coated and NW textured solar cells and SEM image of NWs in contact with top electrode. Electrical characterizations of ARC coated and NW textured solar cells for (b) photovoltaic conversion efficiencies, (c) external quantum efficiencies and (d) current density-voltage characteristics with different NW lengths [24].



## CHAPTER 2

### SILICON NANOWIRE NETWORK METAL-SEMICONDUCTOR-METAL (MSM) PHOTODETECTORS

#### 2.1 INTRODUCTION

The use of Si NWs in photodetection is an emerging field since these nanostructures offer numerous opportunities for photodetector technology. NWs offer thin active regions, which would be interesting for photodetector technology due to following reasons. First, thinner active regions shorten the carrier transit time. Decreased carrier transit time would result in faster detector response although it decreases absorption and quantum efficiency. Second, thin layers allow the fabrication of miniaturized devices with greater structural compatibility for device integration. This would lead to devices with energy optimized conditions. Last, thin layer devices may offer flexible applications, which is clearly the future trend. There is a great interest in flexible technology and Samsung<sup>®</sup> already announced a flexible mobile phone named YOUM, using an organic light emitting diode screen (OLED). Hence, application of flexible Si based electronics would be necessary to catch up with the future trends in electronics technology.

##### 2.1.1 NW Configurations used in Photodetection

Integrating NWs for active photon absorbing elements within the photodetectors is essential. The main idea of integration is to place an individual or large number of NWs mechanically. There are two main approaches for the integration that are, direct growth of NWs between two electrodes and transfer printing of the fabricated NWs from mother substrate to a device substrate. The latter approach is also called as pick and place method.

###### 2.1.1.1 Direct Growth

Figure 2.1.1 shows the schematics of different approaches for direct growth method for the integration of NWs into photodetectors. A single NW can be grown between two electrodes as shown in Figure 2.1.1 (a). Figure 2.1.1 (a-d) shows schematics of multiple nanowires between two electrodes as; (b) ordered, (c) random in plane and (d) random with out of plane. Another approach is to grow nanowires vertically as ordered or random as shown in Figure 2.1.1 (e) and (f), respectively. This approach necessitates deposition of an insulating dielectric layer prior to top electrode formation.

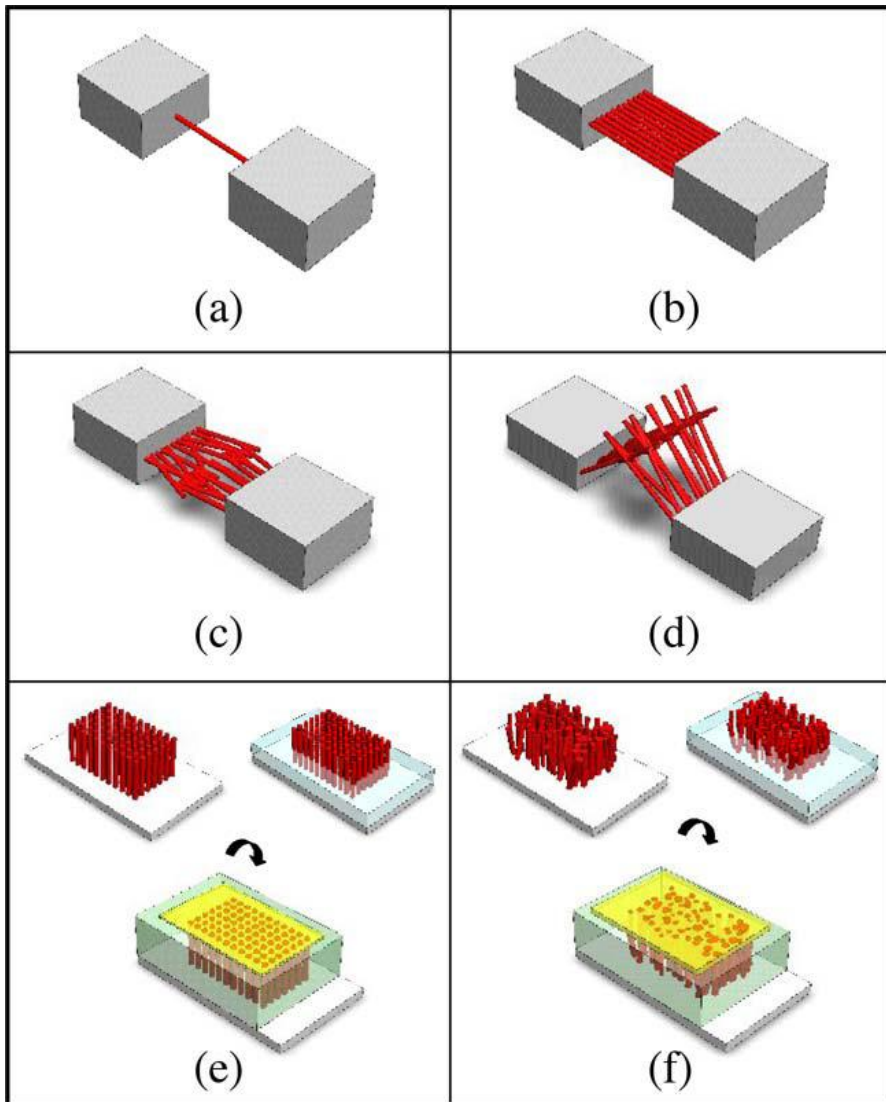


**Figure 2.1.1:** Schematics of different integration routes using direct growth of; (a) single, (b) multiple ordered, (c) multiple random in plane, (d) multiple random out of plane, (e) vertical ordered and (f) vertical random NWs [54].

### 2.1.1.2 Transfer Printing or Pick and Place

For transfer printing or pick and place method, prior to transfer of NWs to device substrate, NWs were grown on the mother substrate. Following growth, either by dry or wet methods, NWs were transferred to the device substrates. Different designs within these approaches are schematically provided in Figure 2.1.2. Figure 2.1.2 (a) show schematic of NWs that were grown ordered as a 2D film and transferred to substrate while preserving their alignment. In (b), vertical arrays of NWs were fabricated randomly and transferred onto substrate without any alignment. In Figure 2.1.2 (c) and (d), following the fabrication of vertical arrays of

ordered NWs, they are transferred onto substrates either as 2D film or as 3D arrays, respectively.

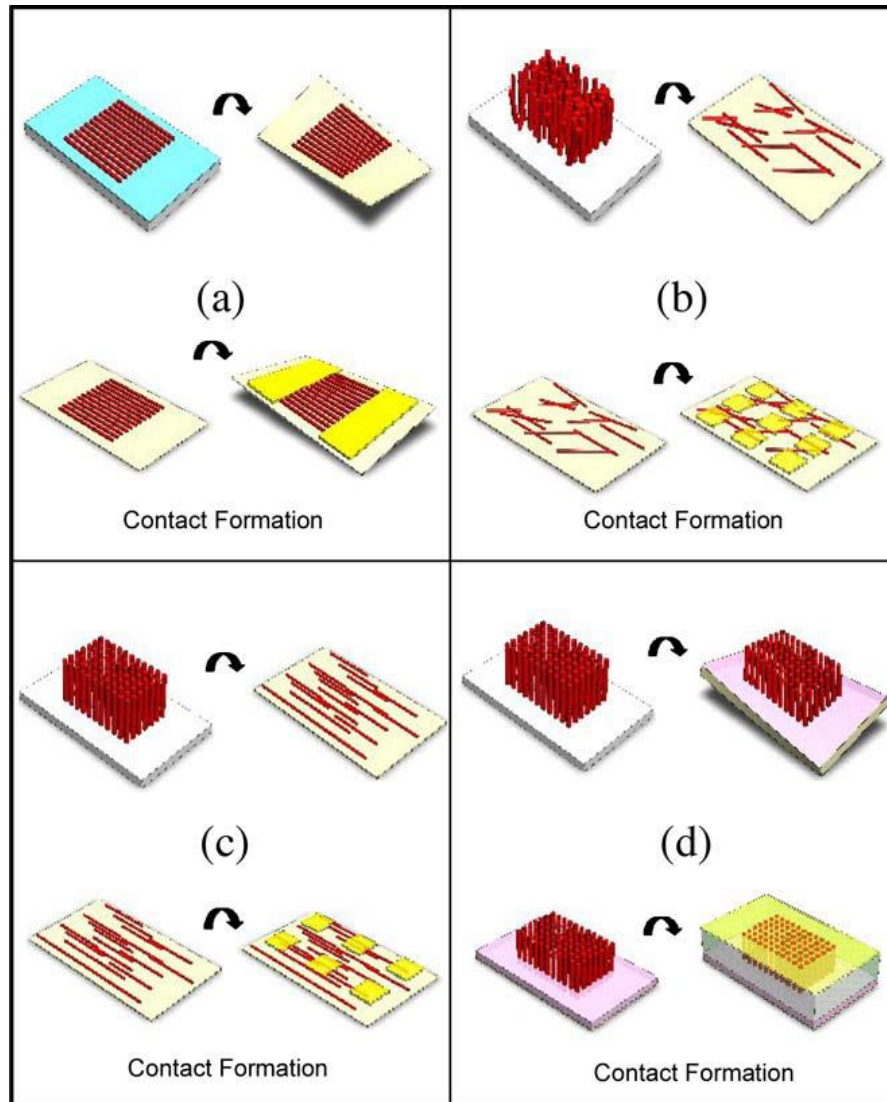


**Figure 2.1.2:** Schematics of different NW integration routes for transfer printing or pick and place; (a) ordered 2D to 2D, (b) random 3D to 2D, (c) ordered 3D to 2D and (d) ordered 3D to 3D [54].

## 2.1.2 Major Photodetector types for Si NWs

### 2.1.2.1 Photodiodes

Nanowires offer a variety of new architectures for photodiode applications. A photodiode can be built with creating a *p-n* junction. The built in electric field between junctions

separates the photogenerated carriers resulting in a net current upon illumination. Homojunction photodiodes are created with the same material; but, different doping types to create  $p-n$  junctions. Heterojunction photodiodes, on the other hand, are the combination of two different materials making  $p-n$  junctions.

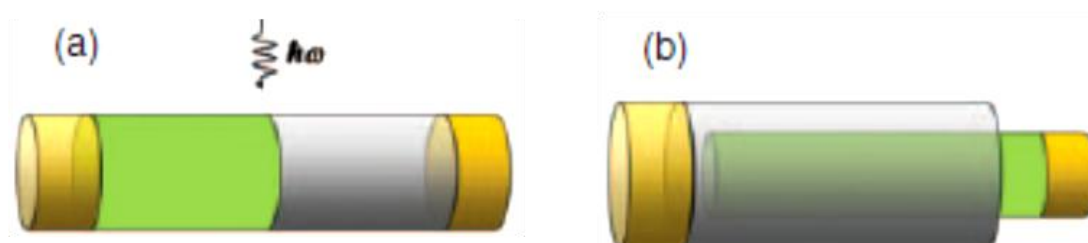


**Figure 2.1.3:** Schematics of (a) axial junction and (b) core-shell radial junction photodiode architectures [55].

### 2.1.2.2 Metal-Semiconductor-Metal (MSM) Photodetectors

Typical MSM photodetectors simply produce electrical signals (i.e. current) through the absorption of photons. Photoabsorption results in the generation of excited photoelectrons and holes that are drifted under the electric field applied externally between the two metal contacts. This kind of photodetectors are quite attractive due to their fast response and low noise performance [56]. Moreover, they store a few minority carriers, which make them suitable for fast switching devices. Up to date, planar MSM photodetectors with Si NWs were formed through the deposition of metallic contacts on both ends of a single NW or arrays of NWs. Schematic structure of these array devices are provided in Figure 2.1.4. These structures suffer from low-photoinduced current [57]. Moreover, the electrical contacts in these devices consist of metallic thin films deposited by vacuum based methods that increase the cost of fabrication and deteriorate the device properties due to the shadowing effect. Some studies have recently been carried out in order to find alternatives to metallic contacts, such as transparent and conducting indium tin oxide (ITO) [41]. However, vacuum deposition necessity, limited indium sources and limited flexibility are a few inherent problems of ITO yet to be solved.

### 2.1.3 Si NW Architectures Used In Photodetector Applications

The use of Si NWs in photodetectors has already been demonstrated in two different forms. The first one utilizes vertical arrays of Si NWs as the active layer of the devices, as shown in Figure 2.1.5 [41, 46, 57]. Figure 2.1.5 (a) shows a metal-insulator-semiconductor (MIS) photodetector fabricated with vertical Si NW arrays [41]. Surface oxide of the NWs served as the insulator layer and ITO were used as metal in the MIS architecture. Although this morphology gives enhanced light harvesting and high quantum efficiencies, the rigidity of the structure prevents flexible applications.

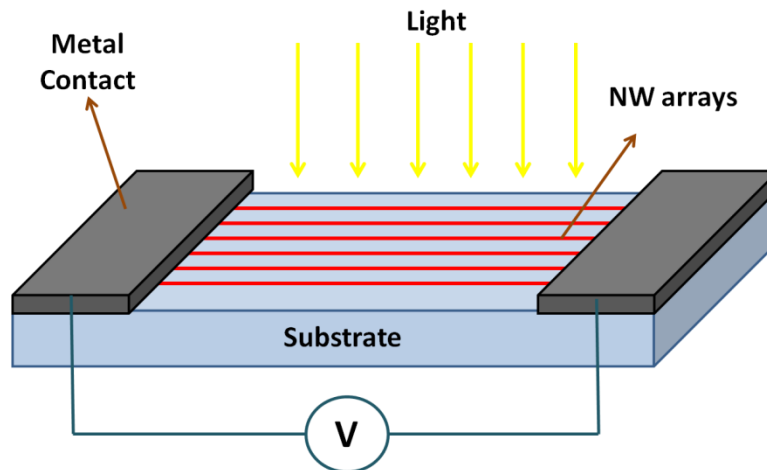


**Figure 2.1.4:** Schematic structure of an MSM photodetector. Bias is applied through metal contacts where in between photoactive region (NWs) is located.

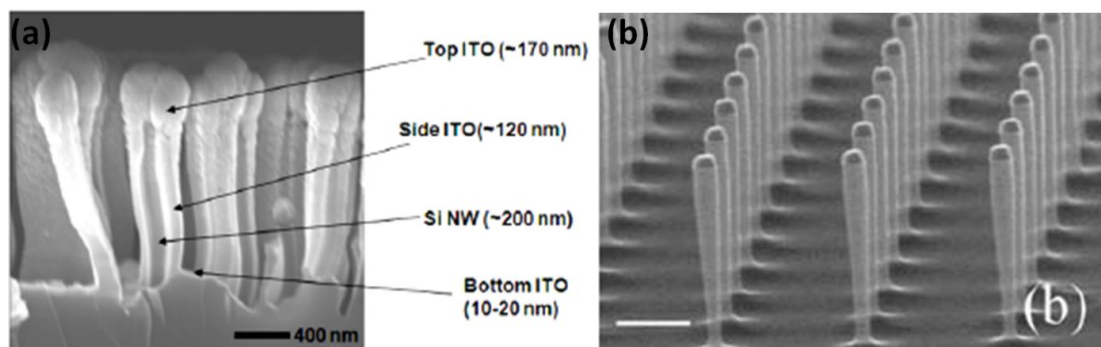


**Figure 2.1.5:** SEM image of vertical arrays of Si NWs used in (a) MIS photodetector [41] and (b) MSM photodetector. Scale bar corresponds to 500 nm [58].

In the second form, planar single/multiple Si NW(s) has been used as the active layer of the devices as shown in Figure 2.1.6. These structures are totally compatible with the integrated optoelectronic systems [58, 59]. They were fabricated through lithographical processes. Flexible photodetectors with Si NWs have been fabricated in this architecture by Oh et al. [59]; however, lithographical methods increased the cost of the process for large scale production. Moreover, the use of thin metallic layers limited the inherent flexibility of the devices.

While vertical arrays of Si NWs suffer from the rigidity of the structure, lithography usage of planar Si NW photodetectors increase the cost of the devices [59]. Fabrication of low-cost and flexible Si NW photodetectors is somehow limited and definitely necessitates novel approaches. Moreover, the new approaches have to decrease the cost of the process and

allow fabrication of flexible devices. These approaches for the case of planar NW networks would be combined with transparent conducting contacts (TCCs) decreasing the cost and allowing flexibility. Among the alternative transparent and conducting contacts, random networks of silver (Ag) NWs could be a promising candidate. These transparent NW electrodes show no shadowing effect as in the case of thin metallic films on devices and offer true flexibility [60-62].

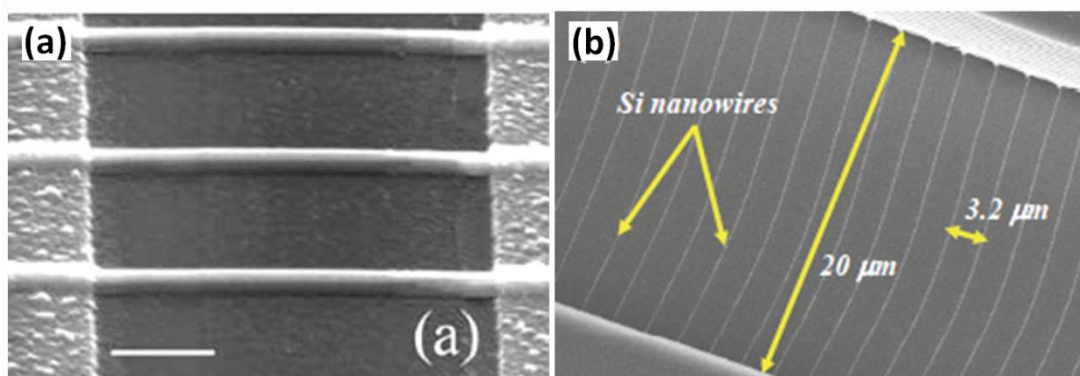


**Figure 2.1.6:** SEM images of planar Si NW arrays in photodetector applications [58, 59].

This chapter reports on the fabrication and characterization of the solution processed Si NW network based MSM photodetectors. Although buckling of Si NWs on elastomeric substrates have been studied [63, 64] and Si NW network based devices have been shown for FET applications [51, 65], these structures had not been studied for flexible photodetection. In order to realize, vertical arrays of Si NWs have been fabricated through simple and low cost MAE method and then transferred onto device substrates in the form of random networks. Ag NWs, on the other hand, were synthesized via the polyol route [66] and spray coated onto device substrates, such as glass and PET. Ag NW networks acted as the electrodes. The channel (gap) within the Ag NW networks was formed via mechanical means. Fabricated MSM photodetectors showed fast response and fully reversible switching behavior. The same structure was obtained on flexible substrates and devices preserved their optoelectrical characteristics upon bending.

## 2.2 EXPERIMENTAL DETAILS

### 2.2.1 Fabrication of Nanowires

All chemicals were purchased from Sigma<sup>®</sup> Aldrich and used without further purification. For the Si NW fabrication, the MAE method, as reported in the introduction part of this thesis and elsewhere, was followed [19]. The cleaning process was applied to Si wafers (400

$\mu\text{m}$  thick,  $\langle 100 \rangle$  orientation, p-type, resistivity 5-10  $\Omega\cdot\text{cm}$ ) prior to etching. Si wafers were cleaned with consecutive sonication in acetone (99.8%), isopropanol (99.8%), and deionized (DI) water baths for 15 min. To remove metal and organic residues from the wafer, boiling piranha solution was prepared by mixing sulfuric acid ( $\text{H}_2\text{SO}_4$ , 95–97%) and hydrogen peroxide ( $\text{H}_2\text{O}_2$ , 35%) by a volume ratio of 3:1 and the samples were immersed into this solution for 1 hour. The samples were dipped into diluted hydrofluoric acid (HF) (38–40%) solution for the removal of native oxide. A MAE solution was prepared by mixing HF (38–40%) and  $\text{AgNO}_3$  (99.5%) at a molar ratio of 4.6 M:0.02 M.

All the etching procedures have been carried out at room temperature with an etching rate of 20  $\mu\text{m}/\text{hour}$ . Following the achievement of the desired NW length, etching was finalized by rinsing samples with DI water. Ag dendrites, which were formed as by-products of MAE, were removed through a nitric acid (DI water 1:3  $\text{HNO}_3$  by vol. ratio) rinse.

Ag NWs were synthesized using the polyol method as reported elsewhere [66]. In a typical experiment, 0.45 M of poly(vinylpyrrolidone) (PVP) (MW = 55,000) and 7 mg of sodium chloride (NaCl) (99.5%) were dissolved in 10 mL ethylene glycol (EG) and heated up 170°C in a silicon oil bath. In the meantime, a 0.12 M  $\text{AgNO}_3$  (99.5%) solution in 5 mL of EG was prepared and added drop-wise into the PVP solution by a syringe pump at a rate of 5 mL/h. The solution was stirred at a rate of 1,000 rpm by a magnetic stirrer throughout the whole process. Following their synthesis, Ag NWs were purified via multiple centrifuging processes (dispersion in acetone and ethanol, 8,000 rpm for 20 min) and then re-dispersed in ethanol. Purified Ag NWs were coated onto glass and PET substrates through spray coating. Following deposition, Ag NW networks were annealed at 200°C for 20 min in order to remove residual PVP and thus decrease the resistance of NWs at junction points.

### 2.2.2 Fabrication of Photodetectors

For the fabrication of devices, Ag NW networks with a transmittance and sheet resistance of 83% (at 550 nm) and 15  $\Omega/\text{sq}$ , respectively, was used as electrodes. A 40  $\mu\text{m}$  gap within the Ag NW network formed by mechanical means (i.e razor blade) served as the channel in photodetectors. Si NW networks were then transferred onto the Ag NW network.

To fabricate Si NW network photodetectors, the native oxide of the Si NWs were removed by a diluted HF (38–40%) rinse (volume ratio 1:20). Afterwards, Si NWs were dispersed in DI water through sonication. Si NW networks were then fabricated through simple vacuum filtration and stamping process. NW density in the network was controlled during vacuum filtration, where a desired amount of solution was filtered. NW density of the networks was determined via ImageJ<sup>®</sup> analysis software using the SEM images.

## **2.3 CHARACTERIZATION METHODS**

### **2.3.1 Scanning Electron Microscopy**

Si NWs and the devices were characterized through a scanning electron microscope (SEM) using FEI<sup>®</sup> Nova Nano SEM 430 microscope operated at 10 kV.

### **2.3.2 Electrical Characterization**

Current-voltage (I-V) characteristics of the photodetectors were obtained using a Keithley 2400 sourcemeter. AM 1.5G solar simulator was used as a light source. Light ON-OFF measurements were conducted at a bias of 5 V. The rise and fall time of the photodetectors ( $1.87 \text{ NW}/\mu\text{m}^2$ ) were measured with an Agilent<sup>®</sup> brand oscilloscope (10 M $\Omega$  oscilloscope probe) using a 1.3 mW Xenon light source (Cermax<sup>®</sup> Xe fiber optic light source) around a 3 mm diameter circle illuminated area and chopped (NewFocus<sup>®</sup> 3501) at 200 Hz under 2.5 V bias. The spectral photoresponsivity of the photodetector with a 10 V bias ( $1.87 \text{ NW}/\mu\text{m}^2$ ) was measured using 100 W QTH lamp (Oriental<sup>®</sup> instruments), Cornerstone 260 1/4m monochromator (Oriental<sup>®</sup> instruments 74100), and Keithley 2440 source meter. The light power was measured using a single channel powermeter (Newport<sup>®</sup> 1936-c).

### **2.3.3 Optical Characterization**

Transmittance measurements were made through the same Xe light source as in the case of electrical characterization and a spectrometer (Ocean Optics<sup>®</sup>). All of the measurements were conducted at atmospheric conditions and room temperature.

## **2.4 RESULTS**

### **2.4.1 Fabrication of Si NWs and Vacuum Filtration Technique**

Photograph on the left and right hand side of Figure 2.4.1 (a) shows Si wafer with vertically aligned NW arrays formed by the MAE process and Si NWs dispersed in DI water following sonication. As shown by the SEM image, the length of Si NWs used in this work was approximately 40  $\mu\text{m}$ . In order to control the density of the Si NWs in the solution, 1  $\text{cm}^2$  area of Si NW containing Si wafer was immersed in a 20 mL of DI Water (18.3 M $\Omega$ -cm) following oxide removal. Only a few seconds of sonication was enough for the rupture of Si NWs from their roots and their consequent dispersion. Further sonication was avoided to prevent NW damage. Si NW dispersion was achieved as evidenced by the brownish color of the solution. The solution was kept at room temperature for a few hours for the precipitation of large NW bundles. Then, the Si NW solution with a known volume was vacuum filtered and a network was formed on a mixed cellulose ester (MCE) membrane as shown in Figure

2.4.1 (b). Following vacuum filtration, Si NW networks were transferred onto substrates through simple stamping processes. A photograph of a semi-transparent Si NW network deposited onto glass substrate is shown in Figure 2.4.1 (b).

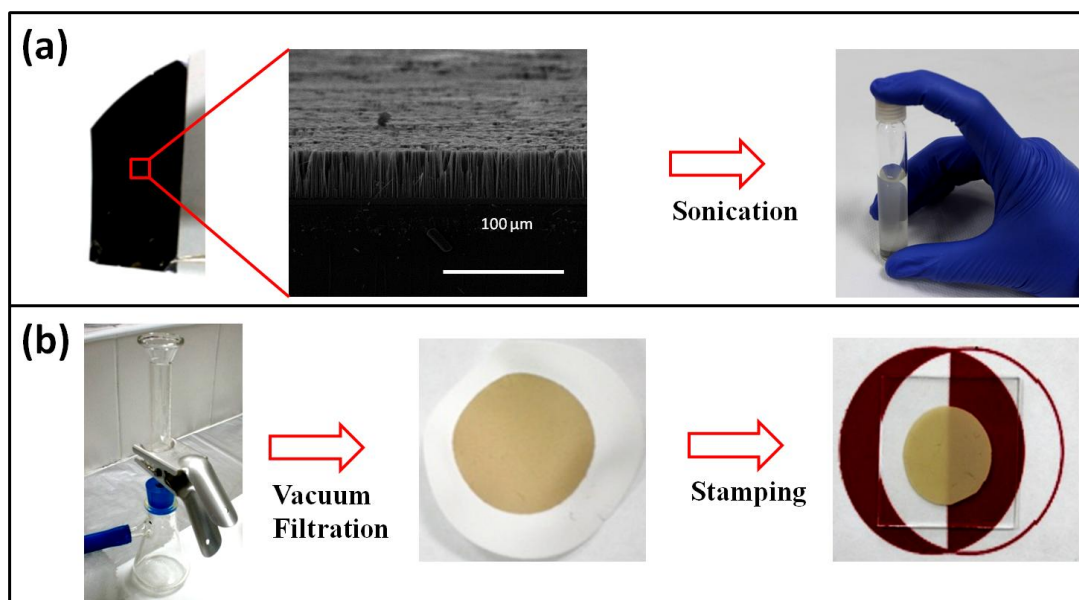


**Figure 2.4.1.** (a) A photograph of Si wafer with Si NW arrays, SEM image of vertically aligned Si NWs and Si NWs dispersed in water. (b) Photographs of the vacuum filtration setup, Si NW networks on filtration membrane and on glass.

## 2.4.2 Density Calculation of NWs and Transmittance result

The NW density was calculated via the Image J<sup>®</sup> analysis software using the SEM images shown in Figure 2.4.2 (a)-(c). NW density was determined to be 0.87, 1.87 and 3.44 NW/ $\mu\text{m}^2$  for the filtered solution volumes of 2.5, 5 and 10 mL, respectively. Variation of the transmittance of Si NW networks with different NW densities are provided in Figure 2.4.2 (d). For comparison, the transmittance spectrum of the Ag NW network was also provided in the same figure. As expected, the transmittance of the NW networks decrease with increasing NW density. Transmittance of the network with a density of 0.87 NW /  $\mu\text{m}^2$  was found to be 40%, whereas that for a density 3.44 NWs /  $\mu\text{m}^2$  was 5% at 550 nm. The Ag NW network has almost 80 % transmittance at the same wavelength.

Inset of the Figure 2.4.3 (a) shows an SEM image of the channel (gap) which was free from Ag NWs following mechanical scratching. SEM image of the MSM structure is given in Figure 2.4.3 (a). MSM structure was obtained through vacuum filtering and stamping of Si NWs onto the channel formed within Ag NW networks. A schematic of the devices fabricated and investigated in this work is provided in Figure 2.4.3 (b). Following the

deposition of the NWs and creating the MSM structure, Ag contact pads were formed by colloidal Ag paste for electrical measurements. A photograph of the finalized device is provided in Figure 2.4.3 (c).

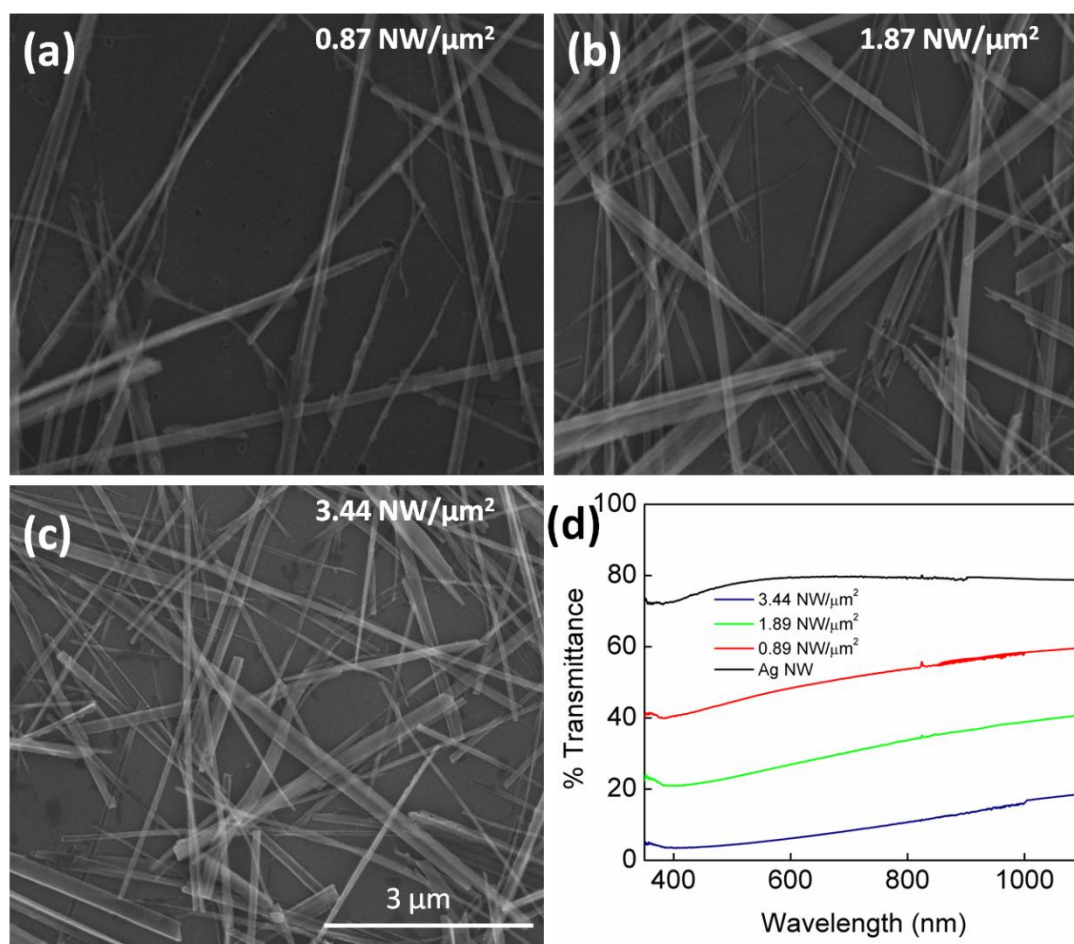


**Figure 2.4.2:** SEM images of Si NW networks with different densities of (a) 0.87, (b) 1.87 and (c) 3.44 NWs /  $\mu\text{m}^2$ . (d) Transmittance spectrum of the NW networks with different NW densities. Transmittance of Ag NW network was provided for comparison.

### 2.4.3 Device Characterization

Figure 2.4.4 (a) shows the photoresponsivities of the Si NW network photodetectors within the wavelength range of 400 to 1000 nm under a 10 V bias. The photoresponse of the devices decreased with increasing wavelength. There is almost no response at 1000 nm since the band gap of Si is around 1100 nm.

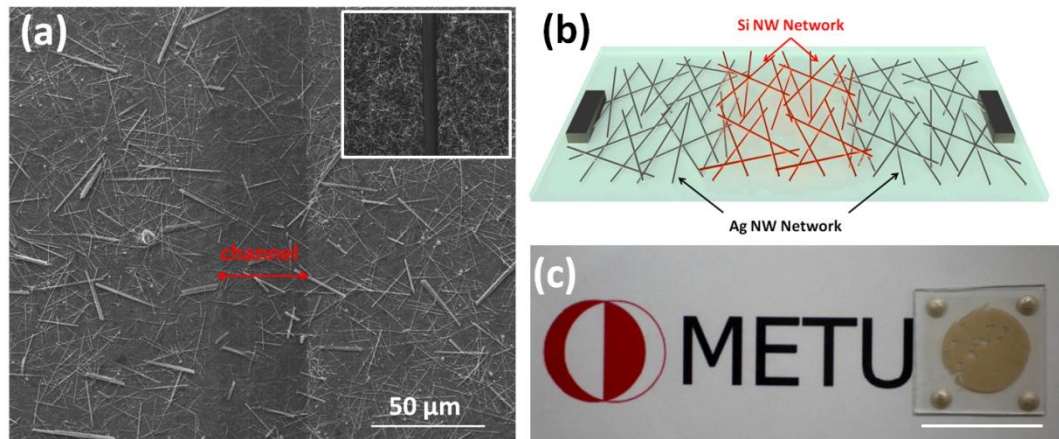


**Figure 2.4.3:** (a) SEM image of the MSM structure. Inset shows that the channel gap was free from Ag NW prior to Si NWs transfer. (b) Representative device architecture and (c) photograph of the final device and scale bar corresponds to 2.5 cm.

The decrease in the responsivity could be attributed to lower photon energies and decreased absorption at longer wavelengths (see Figure 2.4.2 (d)). I–V measurements showed that fabricated MSM photodetectors had a small Schottky barrier at low voltages due to semiconductor NW-NW junctions in the network devices, as shown in Figure 2.4.4 (b).

From the light ON/OFF measurements, photodetectors were found to exhibit fully reversible switching behavior, as shown in Figure 2.4.4 (c). We also see that both the dark and photocurrent of the devices increase with NW density. The increase in the dark current was a result of the creation of alternative conduction paths within the random Si NW network. The enhancement in the photocurrent, on the other hand, is due to enhanced carrier generation from the increased number of NWs in the active layer of the device.

The rise and fall time (dynamic response) of the devices, as shown in Figure 2.4.4 (d), were measured under a 5 V bias. The rise time of the device was determined by measuring the time necessary for the current to increase from 10% to 90% of its saturation value, whereas the fall time was defined as the time necessary for the current to decrease from 90% to 10% of its saturation value. The rise time was found to be 0.43 milliseconds, while the fall time was 0.58 milliseconds. The fall time was relatively high compared to the rise time, which could be related to the deep trap levels created by the defects on the NW surface. The surface passivation of the NWs could be utilized as a solution to improve the photoresponsivity and dynamic response of the devices. A comparison can be made with Si photodiodes fabricated by Li et al. [67] using high quality float zone Si substrates. The typical rise and fall times of 0.55 and 0.3 milliseconds were obtained in this device, respectively. This signifies that our devices exhibit competitive dynamic response values compared to that of the typical Si photodiodes. On the other hand, photodetectors utilizing Si NW arrays with a vertical structure showed higher responsivity with a faster dynamic response [41, 57]. These superior

characteristics were due to better light trapping, higher carrier generation and collection efficiencies owing to the vertical NW structure. Moreover, the collection efficiency was enhanced in these vertical structures due to the reduced carrier entrapment at the NW-NW junctions. Since the NW arrays were not detached from the substrate, collection efficiencies were also considerably high. Compared to this vertically aligned system, the NW network photodetectors studied in this work exhibit slightly lower responsivity and slower temporal response. Light trapping is less pronounced for planar NW network devices (as evident from the color of the samples) and therefore, results in poor light absorption and less carrier generation.

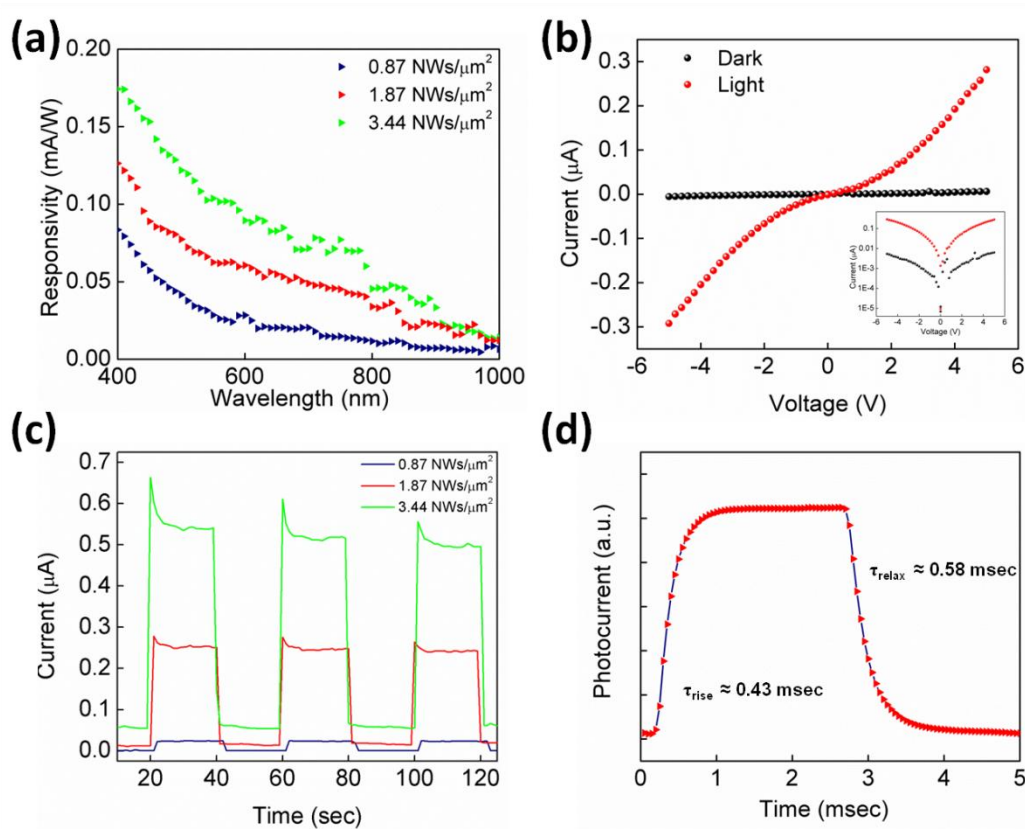


**Figure 2.4.4:** (a) Photore sponsivities with different NW densities under a 10 V bias. (b) I-V characteristics of the device (1.87 NWs/μm<sup>2</sup>). Inset is the logarithmic plot. (c) Light ON-OFF measurements with different NW densities under 5 V bias and (d) dynamic response behavior (1.87 NWs/μm<sup>2</sup>) under a 5 V bias.

In addition, the trapping of photogenerated carriers at the adjacent NW-NW junctions deteriorated the charge collection efficiency of the fabricated photodetectors. However, NW networks offer easy and cost-effective fabrication, partial transparency and flexibility. The

combination of these properties within a photodetector structure could only be realized through the use of planar NW networks. Further optimization studies primarily including surface passivation would improve the device performance.

#### **2.4.4 Flexible MSM Photodetector**

In order to test the flexibility of the MSM photodetectors, the devices ( $1.87 \text{ NW}/\mu\text{m}^2$ ) fabricated on PET substrates underwent a bending test while measuring their optoelectronic properties. The photoconductor performance was recorded as a function of number of bending cycles for a fixed bending curvature of 1 cm. Figure 2.4.5 (a) shows the light ON/OFF measurements upon bending. The reproducible ON/OFF characteristics were obtained with at least an order of magnitude lower current compared to devices on glass substrates. The I-V characteristics of the device both in the dark and illuminated case are shown in Figure 2.4.5 (b), showing similar behavior as in the case of devices fabricated on glass substrates. The dark and photocurrent of a device measured as a function of bending cycles up to a maximum of 500 are shown in Figure 2.4.5 (c). Bending resulted in a decrease of both the light and dark current of the device during the first 200 cycles; however, further increase in the bending cycles did not lead to any change in the current. The decrease in the dark and photocurrent could be due to the loss of mechanical contacts between Si NW junctions and also Ag and Si NWs. After 200 cycles, bending did not lead to any further loss in contacts and therefore, a stable value was achieved. Photograph of the bent device is given in Figure 2.4.5 (d).

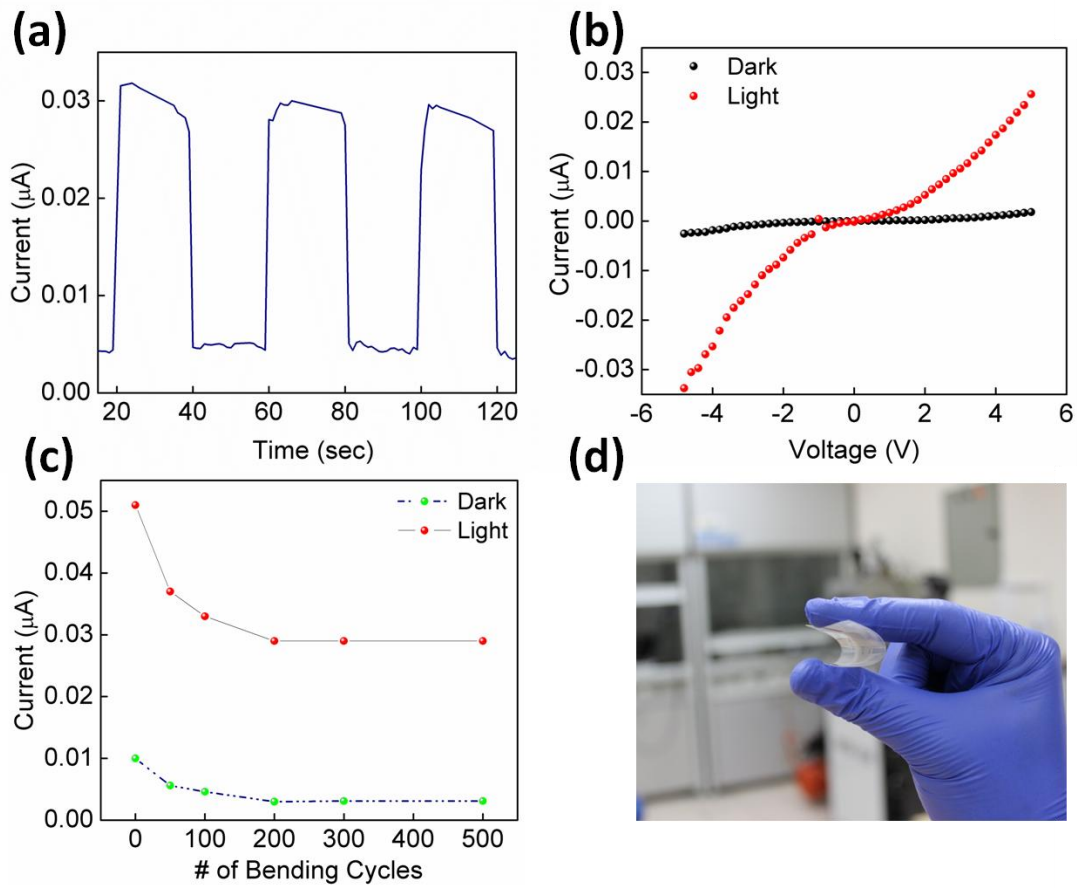


**Figure 2.4.5:** (a) Light ON-OFF measurements under 5 V bias showing that the device is operational upon bending. (b) I-V characteristics of the bent device. (c) Dark/light currents under a bias of 5 V showing stability of the devices in the investigated range. (d) Photograph of a flexible device at a bending radius of 1 cm. A NW density of  $1.87 \text{ NW}/\mu\text{m}^2$  was used for flexible devices.

## CHAPTER 3

### SILVER NANOPARTICLE DECORATED SILICON NANOWIRES FOR LOCALIZED SURFACE PLASMON RESONANCES

#### 3.1 INTRODUCTION

##### 3.1.1 Light and Metal Nanoparticle Interactions

Plasmons through the use of metallic nanoparticles have been investigated for various applications including molecular sensing [68, 69], photonics [70, 71] and solar cells [72, 73]. Incident electromagnetic wave can interact with metallic nanoparticles in two different ways. These are far-field effect and near-field effect, as shown in Figure 3.1.1 (a) and (b), respectively. In the former, nanoparticles might act as scattering elements for the incident light. Light is coupled into the medium underneath the nanoparticles leading to the trapping of the light into the medium. For optical applications, light trapping improves absorption in devices. This far-field effect of plasmonic particles gained special interest especially for thin film devices.

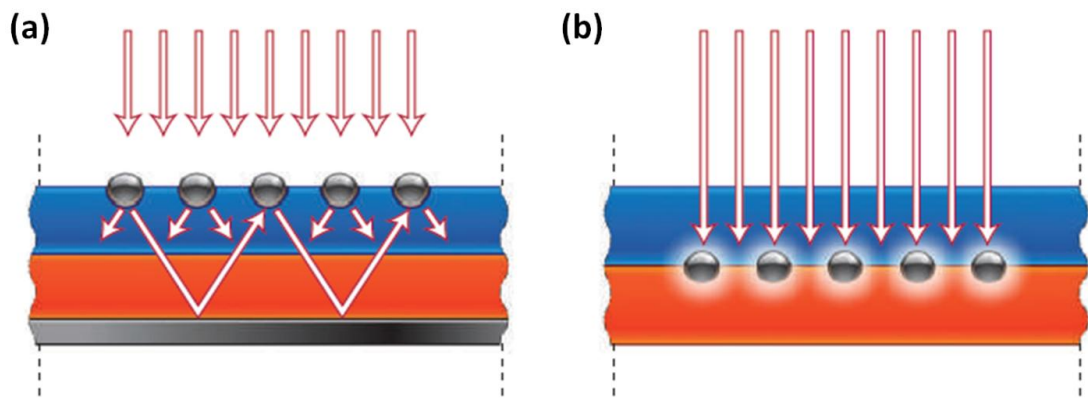


**Figure 3.1.1:** Light-metal nanoparticle interaction, (a) scattering of light by far-field effect and (b) enhancement of electromagnetic field close to the metal nanoparticle by near-field effect [74].

Second, the excitations and enhancements in the electromagnetic field in the vicinity of the metal nanoparticle may occur, as shown in Figure 3.1.1 (b). In this case, metallic nanoparticles act as subwavelength antennas. These antennas couple the incident electromagnetic field creating near-field effect around of the metal nanoparticles. Moreover,

for the case of solar cells, these coupled fields enhance the generation of charge carriers leading to improvements in solar conversion efficiency.

Figure 3.1.2 shows the polarization of free electrons in metal nanoparticles by the interactions with the incident electromagnetic wave. This gives resonance and denoted as localized surface plasmon resonance (LSPR).

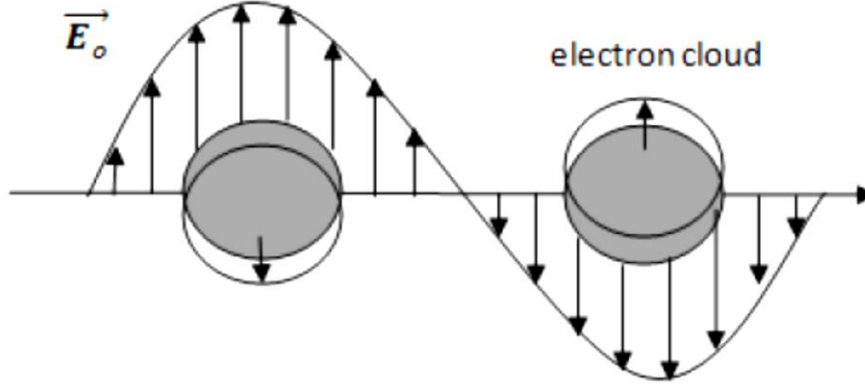


**Figure 3.1.2:** Schematics showing the relative motion of free electrons with the incident electromagnetic field in the resonance condition [68].

Application of the near field effect is often impractical for solar cells. It necessitates metal nanoparticles right at the depletion layer of the  $p$ - $n$  junction, which is quite impractical. Otherwise, the generated carriers via near field effect would recombine before reaching to  $p$ - and  $n$ -side. On the other hand, studying far-field effect is easier compared to near-field effect; since the fabrications of these structures are more reasonable. Hence, this thesis focuses on the far-field effect and LSPR mode.

### 3.1.2 Localized Surface Plasmon Resonances

For a spherical metal, if the incident wavelength is much bigger than the size of the particle, dipolar mode dominates the LSPR mode with polarizability ( $\alpha$ ) given by [75];

$$\alpha = 3\epsilon_0 V \left( \frac{\epsilon_m - \epsilon_s}{\epsilon_m + 2\epsilon_s} \right) \quad (1)$$

, where  $V$  is the particle volume,  $\epsilon_0$  is the vacuum permittivity,  $\epsilon_m$  is the frequency dependent dielectric function of the metal and  $\epsilon_s$  is the dielectric constant of the medium. The overall scattering efficiency,  $Q_{sca}$ , from the particle is the ratio of the scattering cross section,  $C_{sca}$ , to total extinction and can be expressed by;

$$Q_{sca} = C_{sca} / (C_{sca} + C_{abs}) \quad (2)$$

, where the scattering efficiency,  $C_{sca}$ , can be given as [76];

$$C_{sca} = \frac{1}{6\pi} \left(\frac{2\pi}{\lambda}\right)^4 |\alpha|^2 \quad (3).$$

Near the surface plasmon resonance ( $\epsilon_m = -2\epsilon_s$ ), light interacts with the particles at a specific wavelength leading to a strong scattering.

Scattering can be manipulated through changing the polarization parameters given in equation (1). In brief, changing the material type ( $\epsilon_m$ ), surrounding medium ( $\epsilon_s$ ), particle size ( $V$ ) and shape would change the scattering efficiency ( $C_{sca}$ ). Moreover, the physical distance between metal and the medium is also an important parameter for tuning the LSPR wavelength [77, 78].

Scattering is widely used for light trapping in thin film and organic solar cells and particularly in Raman spectroscopy [79-81]. Among plasmonic materials, Au, Ag and Cu are widely used ones since their resonance corresponds to visible frequencies [75]. Ag is one of the most effective metallic nanoparticles used to obtain LSPR mode. It has higher scattering efficiency and lower absorption cross section compared to other metallic plasmonic particles. Furthermore, the scattering/absorption cross sections can be tuned by the particle size. It has been reported that, when the diameter of the Ag nanoparticle exceeds 70 nm, scattering process starts to dominate over absorption [82].

Another nanoscale material system is composed of Si nanowires with new optical and electrical functionalities. Many device systems have been demonstrated with Si nanowires that can be synthesized by various methods. Among these, MAE method stands out as being probably the easiest, solution based route for the fabrication of vertical Si nanowire arrays with desired length and doping characteristics [17, 19]. Successful application of this technique to crystalline Si solar cells with industrial size has been recently demonstrated [24]. There are two alternative pathways in the MAE process; in one-step etching, an aqueous solution of Ag ions together with hydrofluoric acid is used, while in the two-step etching that is an earlier version of this method, a second solution step that contains hydrogen peroxide is utilized. This solution catalyzes the etching of Si underneath the Ag particles.

This chapter reports on the investigation of the scattering behavior of Ag nanoparticle decorated Si NWs. Vertical arrays of Si NWs were fabricated with one-step and two-step MAE method. Si NWs were decorated with Ag nanoparticles via thermal evaporation and subsequent annealing processes. The scattering behavior of the Ag nanoparticle decorated Si NWs were investigated through reflectance measurements.

## **3.2 EXPERIMENTAL DETAILS**

### **3.2.1 Fabrication of Nanowires**

For the Si NW fabrication steps, similar to the ones reported in the previous chapter was followed. For one-step etching, MAE solution was prepared by mixing HF (38-40%) and AgNO<sub>3</sub> (99.5%) at a molar ratio of 4.6 M:0.02 M. For two step etching, seed solution was prepared by mixing HF (38-40%) and AgNO<sub>3</sub> (99.5%) at a molar ratio of 5 M:0.005 M AgNO<sub>3</sub>. The samples were then immersed into the seed solution for 1 minute to allow Ag nanoparticle nucleation on the substrate surface. Then, the samples were removed from solution, rinsed, gently dried with N<sub>2</sub> gas and placed into second solution prepared by mixing 5 M HF and 0.5 M H<sub>2</sub>O<sub>2</sub>. All etching procedures have been carried out at room temperature. After the achievement of the desired NW length, etching was stopped by rinsing samples with DI water. Ag dendrites, which were formed as by-products of MAE, were removed through a nitric acid (DI water 1:3 HNO<sub>3</sub> by vol. ratio) rinse.

### **3.2.2 Silver Nanoparticle Decoration**

Ag nanoparticle decoration was achieved through thermal evaporation. Ag evaporation was started at a base pressure of 10<sup>-6</sup> torr and achieved at a rate of 0.8 Å/seconds. Samples were then annealed at 600 °C for one hour in a vacuum furnace under argon atmosphere. Although evaporation of Ag onto Si NWs directly results in the formation of Ag nanoparticles on NW surfaces, annealing was found to be necessary to obtain more discrete and spherical particles through Ostwald ripening.

## **3.3 CHARACTERIZATION METHODS**

### **3.3.1 Scanning Electron Microscopy (SEM)**

Si NW samples were characterized through a scanning electron microscope (SEM) using FEI<sup>®</sup> Nova Nano SEM 430 microscope operated at 10 kV.

### **3.3.2 Transmission Electron Microscopy (TEM)**

Surface morphologies of the fabricated Si NWs were investigated through a high resolution transmission electron microscope (HRTEM JEOL<sup>®</sup> TEM 2100 F microscope operated at 200 kV). For the preparation of TEM samples, ethanolic solution of NWs were drop casted onto lacey carbon coated Cu grids and allowed to dry in air.

### 3.3.3 Reflectance Measurements

Reflectance measurements were conducted using a 8-inch integrating sphere (Oriel® Model no. 70679NS), halogen light source (100 W), a monochromator (Oriel® Model no: 74100) and a UV enhanced Si photodiode detector (Oriel® Model no: 70356).

### 3.3.4 Fourier Transformed Infrared Spectroscopy (FTIR)

Surface chemistry of the fabricated NWs were investigated through Fourier transform infrared spectroscopy (FTIR) conducted in transmission mode through Bruker® Equinox 55 IR Spectrometer in the mid-infrared range (700 – 1300  $\text{cm}^{-1}$ ).

### 3.3.5 Photoluminescence Spectra (PL)

Photoluminescence (PL) measurements of two-step etched NWs were conducted at room temperature using a 523 nm continuous Nd-Yag laser as an excitation source and response was detected via CCD camera mounted on a monochromator (Oriel® Model no:77700).

## 3.4 RESULTS

### 3.4.1 Morphological, Chemical and Optical Properties of NWs

Morphological differences between the one-step and two-step etched NWs were firstly evaluated through TEM. TEM images of one-step and two-step etched NWs are provided in Figure 3.4.1 (a) and (b), respectively. Diameters of both NWs were around 70 nm. One-step etched NW surface was found to be relatively smooth compared to the two step etched counterpart (see Figure 3.4.1(b)). From this point, smooth surface for one-step etched NWs and rough surface for two-step etched NWs will be used interchangeably. The oxidizing agent ( $\text{H}_2\text{O}_2$ ) in two-step etching clearly deteriorated the surface of the NWs and changed the surface topology. This alteration can be assumed as the main reason for apparent discrepancy between two different etching routes.

Figure 3.4.1 (c) shows the FTIR absorption spectrum of the NWs in the range of 700–1300  $\text{cm}^{-1}$ . Peak centered at 812  $\text{cm}^{-1}$  is related with stretching of O-Si-O bonds showing the bisector of Si atom in between two oxygen atoms [83]. Oxidized hydride deformation mode is located at 880  $\text{cm}^{-1}$  [84]. This deformation related peak does not exist for one-step etched sample, hence oxidized hydride deformation might be correlated with the presence of  $\text{H}_2\text{O}_2$  in the etching solution. Transverse optic (TO) mode of Si-O-Si vibration occurs at 1080  $\text{cm}^{-1}$ , while longitudinal optic (LO) Si-O-Si stretching mode is a shoulder peak located at 1200  $\text{cm}^{-1}$  [85]. This broad vibration mode from 950 to 1250  $\text{cm}^{-1}$  can be correlated to interstitial site occupancy of oxygen atoms in the Si network. This interstitials create vacancies and point defects in the Si matrix and also between Si-O interfaces causing strong absorption at higher

frequencies [86, 87]. Comparing FTIR spectrum of both samples, a clear difference for absorption at high frequencies is apparent. Moreover, this can be further investigated by PL measurements. Figure 3.4.1 (d) shows the PL spectrum of the two-step etched sample. It is a well-known fact that bulk form of Si does not create any light emission due to its indirect band gap ( $E_g \sim 1.1$  eV). One-step etched Si NWs does not give any PL signal either; unless radius of the nanowires are smaller than the Bohr's radius.

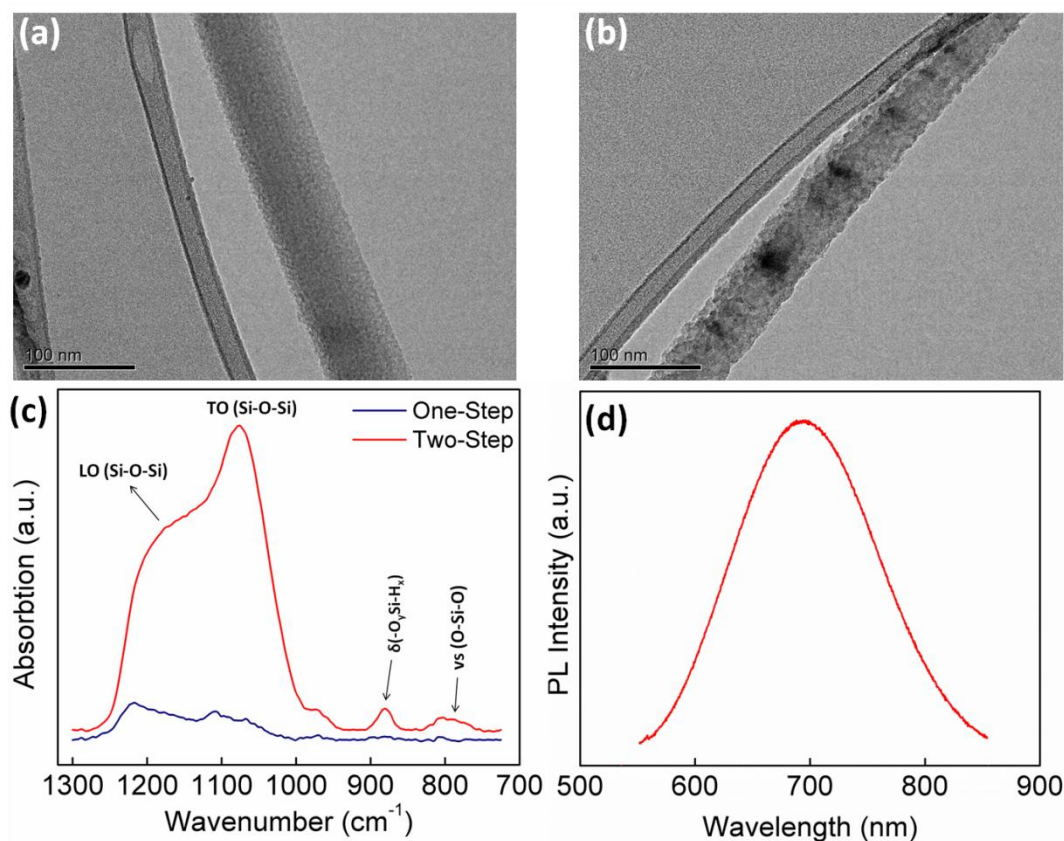


**Figure 3.4.1:** TEM images of (a) one-step and (b) two-step etched Si NW showing surface morphologies. (c) FTIR spectrum of one-step and two-step etched Si NWs. (d) PL spectrum from two-step etched NWs.

On the other hand, there are numerous studies showing photoluminescence from Si NWs fabricated with two-step etching [88, 89]. Within the PL spectrum, signal is centered at 697 nm with a full-width-half-maxima (FWHM) value of 140 nm, which is consistent with the literature [90, 91]. The PL signal is created through radiative recombination on neutral donor-acceptor species from deep trap levels caused by broken Si-O bonds and oxygen related additional localized impurity states created via two-step etching process [90-94]. Hence, it can be concluded that two-step etching degenerates the surface of the NWs creating

oxygen interstitials. Broken bonds and point defects through degeneration enhance infrared absorption at higher frequencies and creates PL signal.

### 3.4.2 Localized Surface Plasmon Resonance

3  $\mu\text{m}$  long Si NWs were fabricated through both one-step and two-step etching routes as explained. Ag thin films with the thicknesses of 12, 24 and 36 nm were deposited onto samples to investigate the LSPR mode and the effect of the particle size. Instead of the Ag nanoparticle size, evaporated film thicknesses were reported in the results part since the determination of the nanoparticle size would yield non-accurate results due to the 3D nature of the samples. However, change in the size and shapes of the nanoparticles were clear enough for discussions made for LSPR modes.

Figure 3.4.2 shows SEM images of Si NWs with evaporated and annealed Ag nanoparticles. As it appears, discrete and spherical Ag nanoparticles were formed upon annealing.

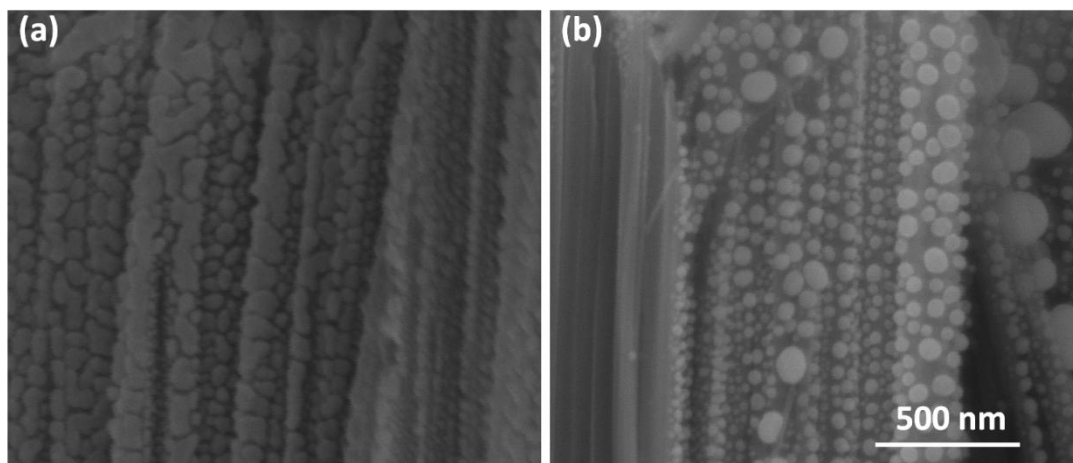


**Figure 3.4.2:** Evolution of discrete and spherical Ag nanoparticles upon annealing. Cross-sectional SEM images of (a) as evaporated and (b) annealed Si NWs. Both scales are the same.

Top-view SEM images of two-step etched samples with Ag thicknesses of 12 and 24 nm are provided in Figure 3.4.3 (a) and (b), respectively. Figure 3.4.3 (c) shows the 36 nm thick Ag decorated two-step etched NWs. Ag nanoparticle size was found to increase with the thickness of the evaporated thin film as evidenced by Figure 3.4.3 (a)-(c). As the thickness increases, nanoparticles form elongated ellipses rather than spheres. SEM image of 36 nm thick Ag deposited one-step etched Si NWs resembles the same structure obtained from two-step etched counterpart, shown in Figure 3.4.3 (d).

Figure 3.4.4 (a) shows the diffuse reflectance spectrum of the Ag decorated Si NWs fabricated through one step etching. Reflection from bare NWs was also provided for

comparison. LSPR peak was observed for the 12 nm Ag deposited sample. Increasing Ag thickness to 24 and 36 nm produced weak and redshifted LSPR peak. It is a known fact that LSPR wavelength redshifts with increasing particle size [77]. The LSPR wavelength for the 24 nm Ag deposited sample could not be determined accurately since the mode was very weak in intensity. However, the LSPR signal,  $\lambda_{LSPR}$  of 36 nm thick Ag deposited sample was determined to be at 495 nm. Figure 3.4.4 (b) shows the enhancement factor, which is calculated using the equation;

$$\Gamma = \frac{(R_{np} - R_{ref})}{R_{ref}} \quad (4).$$

The enhancement factor for 24 nm thick Ag deposited sample was around 0.3 and it was found to increase to 1 for the 36 nm thick Ag deposited sample. On the contrary, when two-step etching route was used, LSPR mode was found to enhance almost 30-fold for 24 nm thick Ag deposited sample, as shown in Figure 3.4.4 (d). Similar to PL case, this enhancement can be attributed to the presence of oxygen related defect sites created by  $H_2O_2$ . These defect sites alter the  $SiO_x$  shell covering crystalline core of the NWs and change the dielectric constant of the effective medium.

Dielectric constant of the medium,  $\epsilon_m$ , changes the polarizability,  $\alpha$ , of the particles according to equation (1). Eventually, scattering cross section,  $C_{sca}$ , and overall scattering efficiency,  $Q_{sca}$ , change with the polarizability of the particle. Enhanced polarizability was obtained from the change in the dielectric constant of effective medium at the NW surface caused by defect sites giving an almost 30-fold enhancement in LSPR mode. Higher dielectric constant of medium and refractive index were known parameters for the increased scattering efficiency [75, 95]; for instance, enhancement in the LSPR mode was obtained by Underwood et al. [96] for Au colloids in a high refractive index medium. However, it is the first time to our knowledge that it is observed for Ag nanoparticle decorated Si NWs. LSPR mode was obtained even for 12 nm thick Ag deposited sample on the contrary to one-step etched counterpart. Increase in Ag thickness redshifted the LSPR wavelength from 438 nm to 477 and to 504 nm for Ag thicknesses of 12, 24 and 36 nm Ag, respectively.

Moreover, increasing the particle size broadened the LSPR peak. The FWHM values, for instance, for the 12, 24 and 36 nm Ag deposited samples were 75.7, 107.8 and 128 nm, respectively. This increase can be attributed to a broader distribution of the particle size and change in the nanoparticle shape from sphere to elongated particles with increasing Ag thickness. Additionally, the enhancement in the resonance mode was found to increase from 15 to 30, as shown in Figure 3.4.4 (d), with changing Ag thickness from 12 to 24 nm. However, there was a slight decrease in the LSPR mode enhancement for 36 nm Ag deposited sample. This could be correlated to the fact that larger particles tend to start multipole oscillations and reduce the overall scattering efficiency [72]. Hence, for a fixed NW length there exists an optimum particle size to get overall enhancement for a wavelength window.

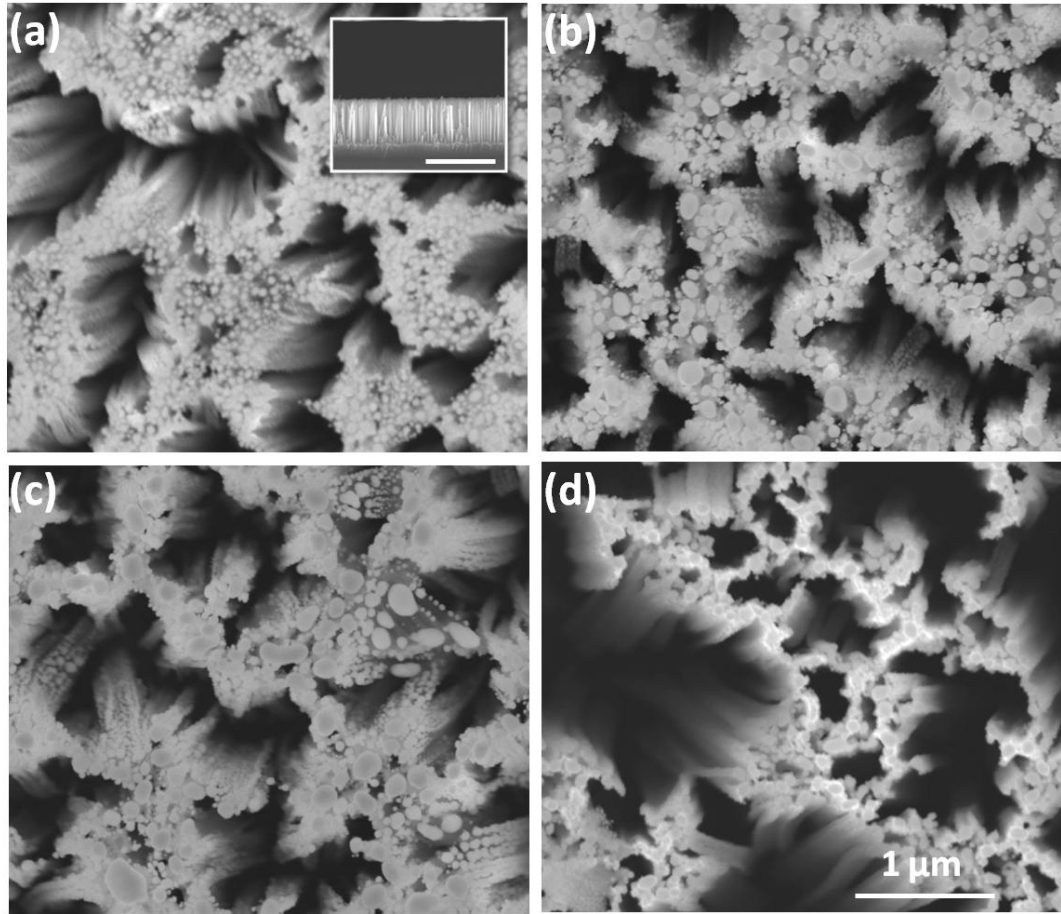


**Figure 3.4.3:** Top-view SEM images of Ag nanoparticle decorated two-step etched Si nanowires with different Ag thicknesses of (a) 12 nm, (b) 24 nm and (c) 36 nm. (d) Top-view SEM image of Ag nanoparticle decorated one-step etched Si nanowires with Ag thicknesses of 36 nm. All scales are the same. Inset shows the 3  $\mu\text{m}$  long vertical arrays of Si NWs fabricated with two-step etching. Inset scale corresponds to 5  $\mu\text{m}$ .

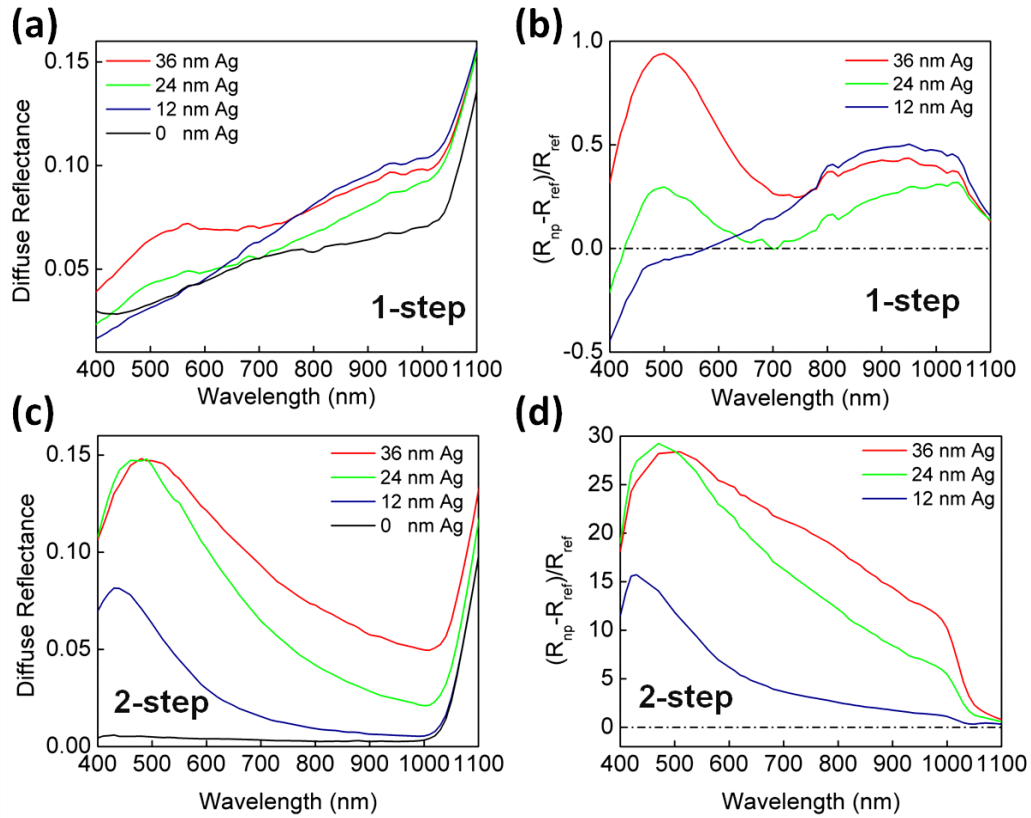


**Figure 3.4.4:** (a) Diffuse reflectance spectrum for 12, 24 and 36 nm Ag deposited samples that are (a) 3  $\mu\text{m}$  long one-step etched Si nanowires and (b) their corresponding spectral enhancement ratios. (c) Diffuse reflectance spectrum for 3  $\mu\text{m}$  long two-step etched Si nanowires and (d) their corresponding spectral enhancement ratios.

The difference in the LSPR mode between one-step and two-step etched samples was also clear through visual inspection. Two-step etched sample with an Ag thickness of 12 nm had a deep blue color as shown in Figure 3.4.5; however, one-step etched counterpart was grayish and there was no color variation upon the change in deposited Ag thickness. For the two-step etched samples, on the contrary, redshift of the mode with increasing Ag thickness could be easily realized. Deep blue color for the 12 nm Ag deposited sample turned greenish showing a redshift in the resonance mode for 36 nm Ag deposited sample. The same color variation was obtained on Ag deposited planar Si samples, which confirmed the strong resonance of our samples [72].

The effect of NW length on the resonance mode was also investigated. 24 nm Ag was evaporated onto 3, 5 and 10  $\mu\text{m}$  long two-step etched Si NWs. Diffuse reflectance spectra for the samples are provided in Figure 3.4.6 (a). For 3  $\mu\text{m}$  long Si NWs,  $\lambda_{SPR}$  was found to be at 479 nm and redshifted to 490 nm for 5  $\mu\text{m}$  long sample. Furthermore, FWHM value of the 3  $\mu\text{m}$  long sample was 109.6 nm and it decreased to 97.7 nm for 5  $\mu\text{m}$  and to 80.8 nm for 10

$\mu\text{m}$  long NWs. The FWHM decreases since the size distribution of the nanoparticles becomes more uniform. This could be correlated to the increased surface area for the deposition of Ag nanoparticles and reduction in the particle-particle interactions. Enhancement factors of the samples are provided in Figure 3.4.6 (b). The enhancement factor increased from 30 to almost 50-fold by changing NW length from 3  $\mu\text{m}$  to 5  $\mu\text{m}$ . Further increase in the NW length to 10  $\mu\text{m}$  diminished the resonance mode since particle-particle interactions become weaker. This suggests that in addition to optimum Ag thickness, NW length also plays an important role in obtaining overall scattering efficiency for three dimensional structures.

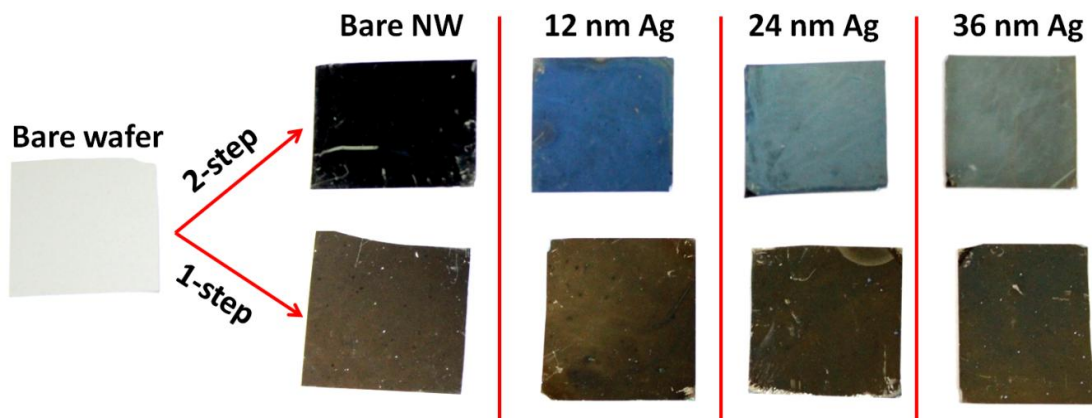


**Figure 3.4.5:** Photographs of one-step (below) and two-step (above) etched Si NWs with different Ag thicknesses.

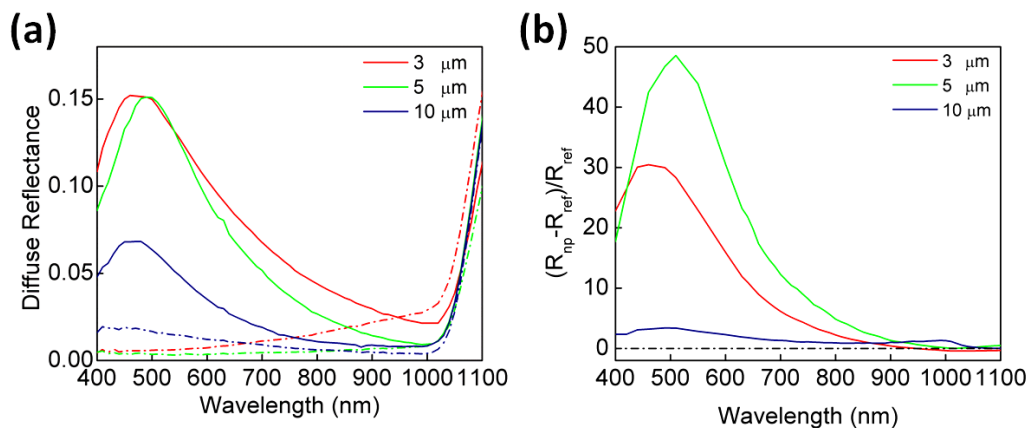


**Figure 3.4.6:** (a) Diffuse reflectance spectra for 24 nm thick Ag deposited 3, 5 and 10  $\mu\text{m}$  long Si NWs. Dashed lines indicate the bare NW. (b) Corresponding spectral enhancement ratios.



## CHAPTER 4

### CONCLUSIONS AND FUTURE RECOMMENDATIONS

#### 4.1 CONCLUSIONS

This thesis is mainly composed of two parts. First part includes the use of Si NWs for photodetectors and the second part includes the use of Si NWs for plasmonics. Si NWs were fabricated through MAE method, which is simple, low cost and solution based. In the first part of the thesis, following fabrication, Si NWs were dispersed in DI water through sonication. Si NW networks were then formed through simple vacuum filtration and stamping process. NW density in the network was controlled during vacuum filtration, where a desired amount of solution was filtered. Fabricated photodetectors showed partial transparency and fully reversible switching behavior (with a switching ratio of  $\sim 20$ ). The dark and photocurrent of the devices increased with NW density. The increase in the dark current was a result of the creation of alternative conduction paths in the random Si NW network. The enhancement in the photocurrent, on the other hand, was due to enhanced carrier generation from the increased number of NWs in the active medium of the device. Fabricated devices showed fast dynamic response with a rise and fall time of 0.43 and 0.58 milliseconds, respectively. Almost the same device characteristics were obtained for the devices fabricated on flexible substrates. Moreover, the dark and photocurrent of the flexible devices were measured as a function of bending cycles up to a maximum of 500. Bending resulted in a loss of dark and light current for the first 200 cycles. However, further increase in the number of bending cycles did not lead to any changes in the current. The results presented provide the basis for the fabrication of cost-effective and flexible photodetectors using Si NWs in a network form. The Si NW networks offer flexibility to the “Silicon World” and could certainly be used for the fabrication of other optoelectronic and sensing devices.

In the second part of the thesis, investigation of the LSPR on Si NWs has been done. For this purpose, vertical arrays of Si NWs were fabricated via one-step and two-step MAE method. NWs fabricated with two-step etching route had rough and degenerated surfaces as revealed by TEM analyses. FTIR spectrum of the two-step etched sample showed strong absorption compared to one-step etched counterparts at high frequencies ( $950\text{--}1250\text{ cm}^{-1}$ ). Strong absorption was correlated to the defect sites created by oxygen interstitials in Si matrix. Moreover, these defect sites emitted visible light by band-to-band radiative recombination confirmed by PL measurements. PL signal was centered at 697 nm consistent with the literature. Furthermore, LSPR of the NWs was investigated upon Ag nanoparticle decoration. Two-step etched NWs showed an almost 30-fold enhanced LSPR mode, while that for one-step etched samples were only 0.3 for an Ag thickness of 24 nm. Enhancement increases to 50-fold increasing the NW length to 5  $\mu\text{m}$  for two-step etched samples. This

distinct enhancement was attributed to the increased dielectric constant of the effective medium around the NWs caused by defect sites. To get an overall enhancement in LSPR mode, NW length and Ag thickness were found to be important parameters. Enhancement obtained in the LSPR mode by two-step etched Si NWs, as investigated in the second part of the thesis, is quite promising for optoelectronic and photonic devices.

## **4.2 FUTURE RECOMMENDATIONS**

In the first part of this thesis, it is proven that Si NWs may become the key element for the flexible optoelectronic applications. Moreover, alignment of the NWs during transfer may yield better photodetection properties. Aligned NWs in the devices may allow better understanding of photodetection physics. As it was discussed, NW-NW junctions trap the carriers resulting in a decreased photoresponse and low detector speed. Hence, horizontal alignment may reveal the behavior of the junctions. Combination of alignment with surface passivation of the NWs may further improve the detector speed and photoresponse. Since the longer wavelengths require thicker active area for absorption, thicknesses of NWs in the active area cannot satisfy this requirement. Light trapping may increase the absorption of light while preserving the device thickness. Since Si does not absorb most of the infrared light, plasmonic antennas may absorb the light and inject the excited carriers to the NWs. Hence, plasmonic application of NW PDs might be an exciting field to study.

In the second part of this thesis, it is revealed that vertical arrays of Si NWs fabricated via two-step etching enhance the far-field effect of plasmonic particles. Moreover, simulations of the discussed system may confirm the results. Investigation of the near-field effect of these NWs would be a next step to clarify effect of two-step etching explained in this thesis. Near-field effect may be studied building a radial junction solar cell, since placement of plasmonic particles into the depletion region is possible for the NW case, it would be an exciting research to study plasmonic enhancements for the radial junction solar cells.

## REFERENCES

1. Tanaka, T. and S. Hara, *Thermodynamic evaluation of binary phase diagrams of small particle systems*. Zeitschrift Fur Metallkunde, 2001. **92**(5): p. 467-472.
2. Lim, W.H., F.A. Zwanenburg, H. Huebl, M. Mottonen, K.W. Chan, A. Morello, and A.S. Dzurak, *Observation of the single-electron regime in a highly tunable silicon quantum dot*. Applied Physics Letters, 2009. **95**(24).
3. Zrazhevskiy, P. and X.H. Gao, *Multifunctional quantum dots for personalized medicine*. Nano Today, 2009. **4**(5): p. 414-428.
4. Prinz, G.A., *Spin-Polarized Transport*. Physics Today, 1995. **48**(4): p. 58-63.
5. Tilke, A.T., F.C. Simmel, H. Lorenz, R.H. Blick, and J.P. Kotthaus, *Quantum interference in a one-dimensional silicon nanowire*. Physical Review B, 2003. **68**(7).
6. Jie, J.S., W.J. Zhang, K.Q. Peng, G.D. Yuan, C.S. Lee, and S.T. Lee, *Surface-Dominated Transport Properties of Silicon Nanowires*. Advanced Functional Materials, 2008. **18**(20): p. 3251-3257.
7. Zhao, X.Y., C.M. Wei, L. Yang, and M.Y. Chou, *Quantum confinement and electronic properties of silicon nanowires*. Physical Review Letters, 2004. **92**(23).
8. Cui, Y. and C.M. Lieber, *Functional nanoscale electronic devices assembled using silicon nanowire building blocks*. Science, 2001. **291**(5505): p. 851-853.
9. Liang, D. and J.E. Bowers, *Photonic integration: Si or InP substrates?* Electronics Letters, 2009. **45**(12): p. 578-580.
10. Wagner, R.S. and W.C. Ellis, *Vapor-Liquid-Solid Mechanism Of Single Crystal Growth ( New Method Growth Catalysis From Impurity Whisker Epitaxial Large Crystals Si E )*. Applied Physics Letters, 1964. **4**(5): p. 89.
11. Buttner, C.C., N.D. Zakharov, E. Pippel, U. Gosele, and P. Werner, *Gold-enhanced oxidation of MBE-grown silicon nanowires*. Semiconductor Science and Technology, 2008. **23**(7).

12. Holmes, J.D., K.P. Johnston, R.C. Doty, and B.A. Korgel, *Control of thickness and orientation of solution-grown silicon nanowires*. Science, 2000. **287**(5457): p. 1471-1473.
13. Morales, A.M. and C.M. Lieber, *A laser ablation method for the synthesis of crystalline semiconductor nanowires*. Science, 1998. **279**(5348): p. 208-211.
14. Martinez, R.V., J. Martinez, and R. Garcia, *Silicon nanowire circuits fabricated by AFM oxidation nanolithography*. Nanotechnology, 2010. **21**(24).
15. Fu, Y.Q., A. Colli, A. Fasoli, J.K. Luo, A.J. Flewitt, A.C. Ferrari, and W.I. Milne, *Deep reactive ion etching as a tool for nanostructure fabrication*. Journal of Vacuum Science & Technology B, 2009. **27**(3): p. 1520-1526.
16. Li, X. and P.W. Bohn, *Metal-assisted chemical etching in HF/H<sub>2</sub>O(2) produces porous silicon*. Applied Physics Letters, 2000. **77**(16): p. 2572-2574.
17. Peng, K.Q., Y.J. Yan, S.P. Gao, and J. Zhu, *Synthesis of large-area silicon nanowire arrays via self-assembling nanoelectrochemistry*. Advanced Materials, 2002. **14**(16): p. 1164-1167.
18. Peng, K.Q., J.J. Hu, Y.J. Yan, Y. Wu, H. Fang, Y. Xu, S.T. Lee, and J. Zhu, *Fabrication of single-crystalline silicon nanowires by scratching a silicon surface with catalytic metal particles*. Advanced Functional Materials, 2006. **16**(3): p. 387-394.
19. Ozdemir, B., M. Kulakci, R. Turan, and H.E. Unalan, *Effect of electroless etching parameters on the growth and reflection properties of silicon nanowires*. Nanotechnology, 2011. **22**(15).
20. Wang, N., Y. Cai, and R.Q. Zhang, *Growth of nanowires*. Materials Science & Engineering R-Reports, 2008. **60**(1-6): p. 1-51.
21. Sinitskii, A., S. Neumeier, J. Nelles, M. Fischler, and U. Simon, *Ordered arrays of silicon pillars with controlled height and aspect ratio*. Nanotechnology, 2007. **18**(30).
22. Peng, K.Q., Y. Xu, Y. Wu, Y.J. Yan, S.T. Lee, and J. Zhu, *Aligned single-crystalline Si nanowire arrays for photovoltaic applications*. Small, 2005. **1**(11): p. 1062-1067.

23. Peng, K.Q., H. Fang, J.J. Hu, Y. Wu, J. Zhu, Y.J. Yan, and S. Lee, *Metal-particle-induced, highly localized site-specific etching of Si and formation of single-crystalline Si nanowires in aqueous fluoride solution*. Chemistry-a European Journal, 2006. **12**(30): p. 7942-7947.
24. Kulakci, M., F. Es, B. Ozdemir, H.E. Unalan, and R. Turan, *Application of Si Nanowires Fabricated by Metal-Assisted Etching to Crystalline Si Solar Cells*. IEEE Journal of Photovoltaics, 2013. **3**(1): p. 548-553.
25. Ozdemir, B., M. Kulakci, R. Turan, and H.E. Unalan, *Silicon nanowire - poly(3,4-ethylenedioxythiophene)-poly(styrenesulfonate) heterojunction solar cells*. Applied Physics Letters, 2011. **99**(11).
26. Ozdemir, B., *Fabrication Of Silicon Nanowires By Electroless Etching And Investigation Of Their Photovoltaic Applications*, in *Metallurgical and Materials Engineering*. 2011, Middle East Technical University. p. 107.
27. Kayes, B.M., H.A. Atwater, and N.S. Lewis, *Comparison of the device physics principles of planar and radial p-n junction nanorod solar cells*. Journal of Applied Physics, 2005. **97**(11).
28. Garnett, E.C. and P.D. Yang, *Silicon nanowire radial p-n junction solar cells*. Journal of the American Chemical Society, 2008. **130**(29): p. 9224.
29. Tsakalakos, L., J. Balch, J. Fronheiser, B.A. Korevaar, O. Sulima, and J. Rand, *Silicon nanowire solar cells*. Applied Physics Letters, 2007. **91**(23).
30. Stelzner, T., M. Pietsch, G. Andra, F. Falk, E. Ose, and S. Christiansen, *Silicon nanowire-based solar cells*. Nanotechnology, 2008. **19**(29).
31. Sivakov, V., G. Andra, A. Gawlik, A. Berger, J. Plentz, F. Falk, and S.H. Christiansen, *Silicon Nanowire-Based Solar Cells on Glass: Synthesis, Optical Properties, and Cell Parameters*. Nano Letters, 2009. **9**(4): p. 1549-1554.
32. Hu, L. and G. Chen, *Analysis of optical absorption in silicon nanowire arrays for photovoltaic applications*. Nano Letters, 2007. **7**(11): p. 3249-52.
33. Tian, B.Z., X.L. Zheng, T.J. Kempa, Y. Fang, N.F. Yu, G.H. Yu, J.L. Huang, and C.M. Lieber, *Coaxial silicon nanowires as solar cells and nanoelectronic power sources*. Nature, 2007. **449**(7164): p. 885-U8.

34. Schmidt, V., H. Riel, S. Senz, S. Karg, W. Riess, and U. Gosele, *Realization of a silicon nanowire vertical surround-gate field-effect transistor*. *Small*, 2006. **2**(1): p. 85-88.
35. Goldberger, J., A.I. Hochbaum, R. Fan, and P.D. Yang, *Silicon vertically integrated nanowire field effect transistors*. *Nano Letters*, 2006. **6**(5): p. 973-977.
36. Hochbaum, A.I., R.K. Chen, R.D. Delgado, W.J. Liang, E.C. Garnett, M. Najarian, A. Majumdar, and P.D. Yang, *Enhanced thermoelectric performance of rough silicon nanowires*. *Nature*, 2008. **451**(7175): p. 163-U5.
37. Boukai, A.I., Y. Bunimovich, J. Tahir-Kheli, J.K. Yu, W.A. Goddard, and J.R. Heath, *Silicon nanowires as efficient thermoelectric materials*. *Nature*, 2008. **451**(7175): p. 168-171.
38. Chan, C.K., R.N. Patel, M.J. O'Connell, B.A. Korgel, and Y. Cui, *Solution-Grown Silicon Nanowires for Lithium-Ion Battery Anodes*. *ACS Nano*, 2010. **4**(3): p. 1443-1450.
39. Chan, C.K., H.L. Peng, G. Liu, K. McIlwrath, X.F. Zhang, R.A. Huggins, and Y. Cui, *High-performance lithium battery anodes using silicon nanowires*. *Nature Nanotechnology*, 2008. **3**(1): p. 31-35.
40. Qian, F., S. Gradecak, Y. Li, C.Y. Wen, and C.M. Lieber, *Core/multishell nanowire heterostructures as multicolor, high-efficiency light-emitting diodes*. *Nano Letters*, 2005. **5**(11): p. 2287-2291.
41. Bae, J., H. Kim, X.M. Zhang, C.H. Dang, Y. Zhang, Y.J. Choi, A. Nurmikko, and Z.L. Wang, *Si nanowire metal-insulator-semiconductor photodetectors as efficient light harvesters*. *Nanotechnology*, 2010. **21**(9).
42. Choi, S.J., Y.C. Lee, M.L. Seol, J.H. Ahn, S. Kim, D.I. Moon, J.W. Han, S. Mann, J.W. Yang, and Y.K. Choi, *Bio-Inspired Complementary Photoconductor by Porphyrin-Coated Silicon Nanowires*. *Advanced Materials*, 2011. **23**(34): p. 3979.
43. Zhou, H., G.J. Fang, L.Y. Yuan, C. Wang, X.X. Yang, H.H. Huang, C.H. Zhou, and X.Z. Zhao, *Deep ultraviolet and near infrared photodiode based on n-ZnO/p-silicon nanowire heterojunction fabricated at low temperature*. *Applied Physics Letters*, 2009. **94**(1).

44. Manna, S., S. Das, S.P. Mondal, R. Singha, and S.K. Ray, *High Efficiency Si/CdS Radial Nanowire Heterojunction Photodetectors Using Etched Si Nanowire Templates*. Journal of Physical Chemistry C, 2012. **116**(12): p. 7126-7133.
45. Kim, K.H., K. Keem, D.Y. Jeong, B.D. Min, K.A. Cho, H. Kim, B. Moon, T. Noh, J. Park, M. Suh, and S. Kim, *Photocurrent of undoped, n- and p-type Si nanowires synthesized by thermal chemical vapor deposition*. Japanese Journal of Applied Physics Part 1-Regular Papers Brief Communications & Review Papers, 2006. **45**(5A): p. 4265-4269.
46. Servati, P., A. Colli, S. Hofmann, Y.Q. Fu, P. Beecher, Z.A.K. Durrani, A.C. Ferrari, A.J. Flewitt, J. Robertson, and W.I. Milne, *Scalable silicon nanowire photodetectors*. Physica E-Low-Dimensional Systems & Nanostructures, 2007. **38**(1-2): p. 64-66.
47. Zhang, A., S.F. You, C. Soci, Y.S. Liu, D.L. Wang, and Y.H. Lo, *Silicon nanowire detectors showing phototransistive gain*. Applied Physics Letters, 2008. **93**(12).
48. Yang, C., C.J. Barrelet, F. Capasso, and C.M. Lieber, *Single p-type/intrinsic/n-type silicon nanowires as nanoscale avalanche photodetectors*. Nano Letters, 2006. **6**(12): p. 2929-2934.
49. Cui, Y., X.F. Duan, J.T. Hu, and C.M. Lieber, *Doping and electrical transport in silicon nanowires*. Journal of Physical Chemistry B, 2000. **104**(22): p. 5213-5216.
50. Cui, Y., Z.H. Zhong, D.L. Wang, W.U. Wang, and C.M. Lieber, *High performance silicon nanowire field effect transistors*. Nano Letters, 2003. **3**(2): p. 149-152.
51. Moon, K.J., T.I. Lee, J.H. Choi, J. Jeon, Y.H. Kang, J.P. Kar, J.H. Kang, I. Yun, and J.M. Myoung, *One-Dimensional Semiconductor Nanostructure Based Thin-Film Partial Composite Formed by Transfer Implantation for High-Performance Flexible and Printable Electronics at Low Temperature*. ACS Nano, 2011. **5**(1): p. 159-164.
52. Munzer, K.A., K.T. Holdermann, R.E. Schlosser, and S. Sterk, *Thin monocrystalline silicon solar cells*. IEEE Transactions on Electron Devices, 1999. **46**(10): p. 2055-2061.
53. *Imec and Kaneka Achieve Breakthrough in Developing Next-Generation Heterojunction Solar Cells*. 2012, last visited on 12/06/2012 [cited 2013 20/06/2013]; Available from: [http://www2.imec.be/be\\_en/press/imec-news/imeckanekalargeareaelectroplating.html](http://www2.imec.be/be_en/press/imec-news/imeckanekalargeareaelectroplating.html).

54. Logeeswaran, V.J., J. Oh, A.P. Nayak, A.M. Katzenmeyer, K.H. Gilchrist, S. Grego, N.P. Kobayashi, S.Y. Wang, A.A. Talin, N.K. Dhar, and M.S. Islam, *A Perspective on Nanowire Photodetectors: Current Status, Future Challenges, and Opportunities*. Ieee Journal of Selected Topics in Quantum Electronics, 2011. **17**(4): p. 1002-1032.
55. Soci, C., A. Zhang, X.Y. Bao, H. Kim, Y. Lo, and D.L. Wang, *Nanowire Photodetectors*. Journal of Nanoscience and Nanotechnology, 2010. **10**(3): p. 1430-1449.
56. Osinsky, A., S. Gangopadhyay, B.W. Lim, M.Z. Anwar, M.A. Khan, D.V. Kuksenkov, and H. Temkin, *Schottky barrier photodetectors based on AlGaN*. Applied Physics Letters, 1998. **72**(6): p. 742-744.
57. Adachi, M.M., K. Wang, F. Chen, and K.S. Karim, *Silicon nanowire metal-semiconductor-metal photodetectors*, in *Medical Imaging 2010: Physics of Medical Imaging*, E. Samei and N.J. Pelc, Editors. 2010, Spie-Int Soc Optical Engineering: Bellingham.
58. Zhang, A., S.F. You, C. Soci, D.L. Wang, Y.H. Lo, and Ieee, *Planar and Vertical Si Nanowire Photodetectors*. 2008 Conference on Lasers and Electro-Optics & Quantum Electronics and Laser Science Conference, Vols 1-9. 2008, New York: Ieee. 96-97.
59. Oh, T.Y., S.W. Jeong, S. Chang, K. Choi, H.J. Ha, and B.K. Ju, *The silicon Schottky diode on flexible substrates by transfer method*. Applied Physics Letters, 2013. **102**(2).
60. Aksoy, B., S. Coskun, S. Kucukyildiz, and H.E. Unalan, *Transparent, highly flexible, all nanowire network germanium photodetectors*. Nanotechnology, 2012. **23**(32).
61. De, S., T.M. Higgins, P.E. Lyons, E.M. Doherty, P.N. Nirmalraj, W.J. Blau, J.J. Boland, and J.N. Coleman, *Silver Nanowire Networks as Flexible, Transparent, Conducting Films: Extremely High DC to Optical Conductivity Ratios*. ACS Nano, 2009. **3**(7): p. 1767-1774.
62. Xu, F. and Y. Zhu, *Highly Conductive and Stretchable Silver Nanowire Conductors*. Advanced Materials, 2012. **24**(37): p. 5117-5122.

63. Ryu, S.Y., J.L. Xiao, W. Il Park, K.S. Son, Y.Y. Huang, U. Paik, and J.A. Rogers, *Lateral Buckling Mechanics in Silicon Nanowires on Elastomeric Substrates*. Nano Letters, 2009. **9**(9): p. 3214-3219.
64. Xu, F., W. Lu, and Y. Zhu, *Controlled 3D Buckling of Silicon Nanowires for Stretchable Electronics*. ACS Nano, 2011. **5**(1): p. 672-678.
65. Heo, K., E. Cho, J.E. Yang, M.H. Kim, M. Lee, B.Y. Lee, S.G. Kwon, M.S. Lee, M.H. Jo, H.J. Choi, T. Hyeon, and S. Hong, *Large-Scale Assembly of Silicon Nanowire Network-Based Devices Using Conventional Microfabrication Facilities*. Nano Letters, 2008. **8**(12): p. 4523-4527.
66. Coskun, S., B. Aksoy, and H.E. Unalan, *Polyol Synthesis of Silver Nanowires: An Extensive Parametric Study*. Crystal Growth & Design, 2011. **11**(11): p. 4963-4969.
67. Li, X., J.E. Carey, J.W. Sickler, M.U. Pralle, C. Palsule, and C.J. Vineis, *Silicon photodiodes with high photoconductive gain at room temperature*. Optics Express, 2012. **20**(5): p. 5518-5523.
68. Willets, K.A. and R.P. Van Duyne, *Localized surface plasmon resonance spectroscopy and sensing*, in *Annual Review of Physical Chemistry*. 2007, Annual Reviews: Palo Alto. p. 267-297.
69. Larsson, E.M., J. Alegret, M. Kall, and D.S. Sutherland, *Sensing characteristics of NIR localized surface plasmon resonances in gold nanorings for application as ultrasensitive biosensors*. Nano Letters, 2007. **7**(5): p. 1256-1263.
70. Barnes, W.L., A. Dereux, and T.W. Ebbesen, *Surface plasmon subwavelength optics*. Nature, 2003. **424**(6950): p. 824-830.
71. Hutter, E. and J.H. Fendler, *Exploitation of localized surface plasmon resonance*. Advanced Materials, 2004. **16**(19): p. 1685-1706.
72. Pillai, S., K.R. Catchpole, T. Trupke, and M.A. Green, *Surface plasmon enhanced silicon solar cells*. Journal of Applied Physics, 2007. **101**(9).
73. Catchpole, K.R. and A. Polman, *Plasmonic solar cells*. Optics Express, 2008. **16**(26): p. 21793-21800.

74. Atwater, H.A. and A. Polman, *Plasmonics for improved photovoltaic devices*. Nature Materials, 2010. **9**(3): p. 205-213.
75. Kreibig, U., Vollmer M, *Optical properties of metal clusters*. Vol. 25. 1995, Berlin: Springer.
76. Bohren C F, H.D.R., *Absorption and Scattering of Light by Small Particles*. 2007: Wiley.
77. Kelly, K.L., E. Coronado, L.L. Zhao, and G.C. Schatz, *The optical properties of metal nanoparticles: The influence of size, shape, and dielectric environment*. Journal of Physical Chemistry B, 2003. **107**(3): p. 668-677.
78. Catchpole, K.R. and A. Polman, *Design principles for particle plasmon enhanced solar cells*. Applied Physics Letters, 2008. **93**(19).
79. Akimov, Y.A., K. Ostrikov, and E.P. Li, *Surface Plasmon Enhancement of Optical Absorption in Thin-Film Silicon Solar Cells*. Plasmonics, 2009. **4**(2): p. 107-113.
80. Baek, S.W., J. Noh, C.H. Lee, B. Kim, M.K. Seo, and J.Y. Lee, *Plasmonic Forward Scattering Effect in Organic Solar Cells: A Powerful Optical Engineering Method*. Scientific Reports, 2013. **3**.
81. Anker, J.N., W.P. Hall, O. Lyandres, N.C. Shah, J. Zhao, and R.P. Van Duyne, *Biosensing with plasmonic nanosensors*. Nature Materials, 2008. **7**(6): p. 442-453.
82. Guler, U. and R. Turan, *Effect of particle properties and light polarization on the plasmonic resonances in metallic nanoparticles*. Optics Express, 2010. **18**(16): p. 17322-17338.
83. Swain, B.S., B.P. Swain, S.S. Lee, and N.M. Hwang, *Microstructure and Optical Properties of Oxygen-Annealed c-Si/a-SiO<sub>2</sub> Core-Shell Silicon Nanowires*. Journal of Physical Chemistry C, 2012. **116**(41): p. 22036-22042.
84. Mawhinney, D.B., J.A. Glass, and J.T. Yates, *FTIR study of the oxidation of porous silicon*. Journal of Physical Chemistry B, 1997. **101**(7): p. 1202-1206.

85. Swain, B.S., B.P. Swain, and N.M. Hwang, *Investigation of electronic configuration and plasmon loss spectra in Au-catalyzed silicon nanowire networks*. Journal of Applied Physics, 2010. **108**(7).
86. Swain, B.S., B.P. Swain, and N.M. Hwang, *Chemical surface passivation of silicon nanowires grown by APCVD*. Current Applied Physics, 2010. **10**(3): p. S439-S442.
87. Hu, Q.L., H. Suzuki, H. Gao, H. Araki, W. Yang, and T. Noda, *High-frequency FTIR absorption of SiO<sub>2</sub>/Si nanowires*. Chemical Physics Letters, 2003. **378**(3-4): p. 299-304.
88. Najar, A., A.B. Slimane, M.N. Hedhili, D. Anjum, R. Sougrat, T.K. Ng, and B.S. Ooi, *Effect of hydrofluoric acid concentration on the evolution of photoluminescence characteristics in porous silicon nanowires prepared by Ag-assisted electroless etching method*. Journal of Applied Physics, 2012. **112**(3).
89. Qu, Y.Q., L. Liao, Y.J. Li, H. Zhang, Y. Huang, and X.F. Duan, *Electrically Conductive and Optically Active Porous Silicon Nanowires*. Nano Letters, 2009. **9**(12): p. 4539-4543.
90. Hochbaum, A.I., D. Gargas, Y.J. Hwang, and P.D. Yang, *Single Crystalline Mesoporous Silicon Nanowires*. Nano Letters, 2009. **9**(10): p. 3550-3554.
91. Kuznetsov, A.S., T. Shimizu, S.N. Kuznetsov, A.V. Klekachev, S. Shingubara, J. Vanacken, and V.V. Moshchalkov, *Origin of visible photoluminescence from arrays of vertically arranged Si-nanopillars decorated with Si-nanocrystals*. Nanotechnology, 2012. **23**(47).
92. Godefroo, S., M. Hayne, M. Jivanescu, A. Stesmans, M. Zacharias, O.I. Lebedev, G. Van Tendeloo, and V.V. Moshchalkov, *Classification and control of the origin of photoluminescence from Si nanocrystals*. Nature Nanotechnology, 2008. **3**(3): p. 174-178.
93. Gole, J.L., F.P. Dudel, D. Grantier, and D.A. Dixon, *Origin of porous silicon photoluminescence: Evidence for a surface bound oxyhydride-like emitter*. Physical Review B, 1997. **56**(4): p. 2137-2153.
94. Wolkin, M.V., J. Jorne, P.M. Fauchet, G. Allan, and C. Delerue, *Electronic states and luminescence in porous silicon quantum dots: The role of oxygen*. Physical Review Letters, 1999. **82**(1): p. 197-200.

95. Lunt, E.A.M., M.C. Pitter, M.G. Somekh, and P. O'Shea, *Studying Protein Binding to Conjugated Gold Nanospheres; Application of Mie Light Scattering to Reaction Kinetics*. Journal of Nanoscience and Nanotechnology, 2008. **8**(9): p. 4335-4340.
96. Underwood, S. and P. Mulvaney, *Effect Of The Solution Refractive-Index On The Color Of Gold Colloids*. Langmuir, 1994. **10**(10): p. 3427-3430.